# UC San Diego
## UC San Diego Previously Published Works

**Title**

HSP70 chaperones RNA-free TDP-43 into anisotropic intranuclear liquid spherical shells

**Permalink**

**Journal**

**ISSN**

**Authors**

Yu, Haiyang
Lu, Shan
Gasior, Kelsey
et al.

**Publication Date**

**DOI**

Peer reviewed

# HSP70 chaperones RNA-free TDP-43 into anisotropic intranuclear liquid spherical shells

**Haiyang Yu**[1,†], **Shan Lu**[#1], **Kelsey Gasior**[#2,3,‡], **Digvijay Singh**[4], **Sonia Vazquez-Sanchez**[1], **Olga Tapia**[5,6], **Divek Toprani**[1], **Melinda S. Beccari**[1,7], **John R. Yates III**[8], **Sandrine Da Cruz**[1,9,10], **Jay M. Newby**[11], **Miguel Lafarga**[5,6,12], **Amy S. Gladfelter**[2,13], **Elizabeth Villa**[4], **Don W. Cleveland**[1,7,†]

[1.] Ludwig Institute for Cancer Research, University of California at San Diego, La Jolla, California, USA

[2.] University of North Carolina Chapel Hill, Department of Biology, Chapel Hill, North Carolina, USA

[3.] University of North Carolina Chapel Hill, Department of Mathematics, Chapel Hill, North Carolina, USA

[4.] Division of Biological Sciences, University of California, San Diego, San Diego, California, USA

[5.] "Centro de Investigación Biomédica en Red sobre Enfermedades Neurodegenerativas" (CIBERNED), Madrid, Spain.

[6.] "Instituto de Investigación Sanitaria Valdecilla" (IDIVAL), Santander, Spain

[7.] Department of Cellular and Molecular Medicine, University of California at San Diego, La Jolla, California, USA

[8.] Departments of Molecular Medicine and Neurobiology, The Scripps Research Institute, La Jolla, California, USA

[9.] VIB-KU Leuven Center for Brain & Disease Research, Leuven, Belgium

[10.] Department of Neurosciences, KU Leuven, Leuven, Belgium

[11.] Department of Mathematical and Statistical Sciences, University of Alberta, Edmonton, Alberta, Canada T6G 2G1

[12.] Department of Anatomy and Cell Biology, University of Cantabria, Santander, Spain.

†Corresponding authors: dcleveland@ucsd.edu, haiyang-yu@ucsd.edu.
‡Present address: Florida State University Department of Mathematics, 1017 Academic Way, Tallahassee, FL 32306.

13. Marine Biological Laboratory, Woods Hole, Massachusetts, USA

# These authors contributed equally to this work.

## Abstract

The RNA-binding protein TDP-43 forms intranuclear or cytoplasmic aggregates in age-related neurodegenerative diseases. Here we show that RNA-binding deficient TDP-43 (produced by neurodegeneration-causing mutations or post-translational acetylation in its RNA recognition motifs) drove TDP-43 de-mixing into intranuclear liquid spherical shells with liquid cores. We proposed the name anisosomes for these droplets, whose shells exhibited birefringence, evidence of liquid crystal formation. Guided by mathematical modeling, we identified the major components of the liquid core to be HSP70 family chaperones, whose ATP-dependent activity maintained the liquidity of shells and cores. In vivo proteasome inhibition within neurons, to mimic aging-related reduction of proteasome activity, induced TDP-43-containing spherical shells, which converted into aggregates when ATP levels were reduced. Thus, acetylation, HSP70, and proteasome activities regulate TDP-43 phase separation and conversion into a gel/solid phase.

## Structured Summary

**Background:** Aggregation of the RNA binding protein TDP-43 (TAR DNA-binding protein 43) is a common pathological hallmark shared by several age-related neurodegenerative diseases, including amyotrophic lateral sclerosis (ALS) and frontotemporal dementia (FTD). The predominantly nuclear TDP-43 normally undergoes Liquid-Liquid Phase Separation (LLPS), in which a homogenous solution separates in two compartments resembling oil droplets in vinegar.

**Rationale:** Intranuclear TDP-43 can phase separate under physiological conditions. Cellular stress can induce cytoplasmic TDP-43 liquid droplets, which can transition to a solid state, suggesting that TDP-43 aggregation observed in neurodegeneration could be initiated by LLPS. Mechanisms driving phase separation and aggregation were not known.

**Results:** We identified key regulatory mechanisms of TDP-43 phase separation in cultured cells and in neurons in the rodent nervous system. We found that RNA-binding deficient TDP-43, produced by ALS/FTD-causing mutations or post-translational acetylation in its RNA recognition motifs, phase-separated into anisosomes, droplets with symmetrical liquid spherical shells and liquid cores. RNA-free TDP-43 was found to be enriched in anisosomal shells at concentrations 50-fold higher than surrounding nucleoplasm. Acetylation promoted anisosomal formation by abolishing RNA interaction with TDP-43. Anisosomal shells exhibited birefringence, evidence of a liquid crystal compartment formed from proteins within living cells. Shells were densely packed, as determined with cryo-electron tomography, producing a membraneless, selective barrier to some nuclear proteins and RNAs.

Our mathematical modeling predicted that anisosomes were driven by a core component that self-interacted, weakly bound TDP-43, and did not bind RNA. Guided by this, we used proximity labeling and quantitative proteomics to identify HSP70 chaperones as the major anisosomal core components. HSP70 chaperones selectively bound to and stabilized RNA-unbound TDP-43. Inhibiting ATP-dependent chaperone activity of the HSP70 family or reducing cellular ATP levels induced rapid conversion of TDP-43 anisosomes into uniform gels. Transient proteasome inhibition, mimicking the known reduction in proteasome activity during aging, provoked TDP-43

de-mixing into anisosomes in neurons in rodents. Postmortem ATP reduction was sufficient to convert anisosomes into aggregates similar to those found in neurodegenerative disease.

**Conclusion:** We identified how phase separation of the RNA-binding protein TDP-43 can be regulated through RNA binding, disease-causing mutation, post-translational modification, or chaperone activity inside cells. RNA binding deficient TDP-43 de-mixed into anisosomes whose cores were a "liquid-inside-a-liquid-inside-a-liquid". Chaperone activity of the HSP70 family was required to maintain liquidity of anisosomal shells and cores. When ATP levels fell, anisosomes converted into protein aggregates, consistent with being precursors of the pathological aggregates found in patient brain tissues. These findings suggest an essential partnership between TDP-43 and HSP70 chaperones in driving RNA-unbound TDP-43 phase separation into anisosomes and preventing TDP-43 aggregation.

## Keywords

TDP-43; HSP70; ALS; FTD; liquid-liquid phase separation; cryo-electron tomography; acetylation; anisotropy; anisosome

---

Mislocalization and aggregation of TDP-43 (TAR DNA-binding protein 43), a nuclear RNA-binding protein, is a pathological hallmark shared by several age-related neurodegenerative diseases, including amyotrophic lateral sclerosis (ALS) (1), frontotemporal dementia (FTD) (2), Alzheimer's disease (AD) (3), and the recently defined AD-like variant named "LATE" (limbic predominant age-related TDP-43 encephalopathy) in the oldest individuals (4). TDP-43 functions in pre-mRNA maturation, including splicing (5). Nuclear aggregation of TDP-43 is also found in affected brain regions of FTD and AD patients (6–9), although it has often been overlooked in pathological analyses focused on phosphorylated TDP-43 aggregates found in the cytoplasm.

TDP-43 naturally de-mixes in the nucleus (10), but can be induced by multiple stresses to accumulate in the cytoplasm. Loss of nuclear TDP-43 causes cryptic splicing (11–13) and premature polyadenylation (13), dysregulating many important neuronal genes, including HSPA8 (14), HDAC6 (15), and stathmin-2 (11, 13). The RNA-binding activity of TDP-43 is inhibited by post-translational acetylation on two lysine residues (K145 and K192) (16). Additionally, acetylated TDP-43 accumulates in cytoplasmic aggregates in the nervous systems of ALS patients (16).

A seminal discovery in the last decade was recognition that proteins, nucleic acids, or a mixture of both can de-mix into two phases, a condensed de-mixed phase and a dilute aqueous phase, resembling oil droplets in vinegar, a phenomenon called liquid-liquid phase separation (LLPS) (17). The condensed phase can form membraneless organelles which have been proposed to promote biological functions (18). Discovery that P-granules are de-mixed compartments with liquid behaviour brought widespread recognition to LLPS and its ability to mediate subcellular compartmentalization in a biological context (19). Phase separation has also been proposed for heterochromatin and RNA bodies (17, 19, 20).

LLPS potentially underlies the operational principle governing formation of important organelles and structures, such as centrosomes, nuclear pore complexes, and super enhancers

(21–23). Beyond two-phase LLPS, a condensed phase can further de-mix into an additional internalized gel, such as in the nucleolus (24) or paraspeckles (24–26), gel-like droplets adjacent to liquid P-granules (27), a gel-like core surrounded by a liquid shell (28), or multiphase liquid droplets of an overexpressed TDP-43 in which its RNA-binding domains have been replaced with GFP (29) or simply removed (30). LLPS of proteins, especially RNA-binding proteins, is currently explained by multi-valent interactions of low complexity domains that are intrinsically disordered (31), with no ordered alignments within the condensed liquid phase.

Here we report an interesting LLPS phenomenon, intranuclear droplets with anisotropic liquid spherical shells and liquid cores, driven by RNA-binding compromised TDP-43 produced by its reversible post-translational acetylation, ALS-causing mutations, or proteasome inhibition. It produced close-to-perfect liquid spherical shells with a high TDP-43 concentration and an inner liquid spherical core enriched in HSP70 family chaperones, forming a "liquid-inside-a-liquid-inside-a-liquid". Because of its anisotropy and the differential ("uneven") distribution of TDP-43 within this unique membraneless compartment, we named it "anisosome", from Greek words "ánisos" and "soma", meaning "uneven body". Shells exhibited birefringence, validating them to be liquid crystals that form from protein within a living cell. In vivo proteasome inhibition, to mimic reduction in proteasome activity during aging (32, 33), induced TDP-43-containing anisosomes to convert into aggregates after ATP reduction.

## RNA-binding deficient TDP-43 de-mixes into liquid spherical shells in physiological conditions

TDP-43 contains an N-terminal self-association domain (34, 35), a C-terminal LCD, and two conserved RNA recognition motifs (RRM1 and RRM2). Its RNA-binding capacity can be reduced by ALS or FTD-causing mutations (P112H, K181E or K263E) (36–38) or eliminated by post-translational acetylation of two lysine residues (K145 in RRM1 and K192 in RRM2) (16) or by replacing five phenylalanine residues in the two RRMs that interact with RNA (39) (Fig. 1A). Cell clones were generated in which full length, RNA-binding deficient TDP-43 variants (each fluorescently tagged with clover) could be induced to accumulate from 0.3 to 9 fold the initial physiological TDP-43 level (Fig. S1A–F). Wildtype TDP-43[clover] formed nuclear droplets (Fig.1B), as we have shown before (10). In contrast, each of the RNA-binding deficient TDP-43 variants (including acetylation-mimicking mutant TDP-43[K145Q,K192Q] in which glutamines replaced the two lysines that are acetylated in TDP-43 (16) and hereafter named TDP-43[2KQ]), TDP-43[5FL] (in which five phenylalanines were substituted to leucines (39)), or ALS/FTD causing mutations TDP-43[P112H] (36), TDP-43[K181E] (37) and TDP-43[K263E] (38) formed close-to-perfectly spherical intranuclear droplets in which TDP-43 was enriched in an outer shell but depleted in the center (Figs. 1B, 1C and S1B). This did not require overexpression, as it was found at RNA-binding deficient TDP-43 levels as low as 0.3 times the level of endogenous TDP-43 (Fig. 1D). De-mixing of TDP-43 into spherical shells with apparently hollow cores was true over a broad range of accumulation of each RNA-binding compromised TDP-43 variant (e.g., for TDP-43[2KQ] between 0.3 and 9 fold TDP-43's normal level (Fig. 1D and Figs. S1D

to S1F)). The fraction of spherical shell-containing nuclei (Fig. 1E) and number of the spheres per nucleus depended on the variant (Fig. 1F), likely due to the remaining level of RNA-affinity and the expression level (Figs. 1B and 1D).

Fluorescence Recovery After Photobleaching (FRAP) was used to determine that RNA-binding deficient TDP-43 enriched in spherical shells freely exchanged with TDP-43 in the nucleoplasm (e.g., TDP-43$^{2KQ\text{-clover}}$ - a mimic of acetylated wildtype TDP-43 (16) - recovered after bleaching with a $t_{1/2}$ of 9 sec - Fig. 1G). Use of 3D live cell imaging of intranuclear nuclear droplets containing TDP-43$^{2KQ\text{-clover}}$ (unambiguously identified in Z projections to be enriched in spherical shells – Fig. S1G and Movie S1) revealed that these droplets frequently fused to form larger droplets (Fig. S1H). Furthermore, direct comparison of fluorescence and differential interference contrast (DIC) imaging revealed that these liquid spherical shells could be directly observed in DIC images (Fig. 1H). Live cell DIC imaging (Movie S2) detected abundant, rapid (within 10 seconds) fusion events in which the shells fused with each other, as did the cores, indicating that both shells and cores behave like liquids.

## Deacetylase or proteasome inhibition drives wildtype TDP-43 to form spherical shells

Inhibition of deacetylases (with the pan deacetylase inhibitors trichostatin A (TSA) or vorinostat (a.k.a. SAHA)) in cells with fluorescently tagged TDP-43 (TDP-43$^{WT\text{-clover}}$) replacing endogenous TDP-43 was sufficient to drive it into spherical shells (Fig. S1I). Similarly, increasing acetylation by expression of a known acetyltransferase [the core component of transcription initiation complex CEBP-binding protein (CBP) (40, 41)] also drove TDP-43$^{WT\text{-clover}}$ into spherical droplets (Fig. S1I), whose number increased markedly and morphology became spherical shells after addition of either deacetylase inhibitor.

Because RNA-binding deficient TDP-43 has been reported to be quickly degraded by nuclear proteasomes (42), we reasoned that de-mixing of acetylated TDP-43 could be enhanced by inhibiting the proteasome. Indeed, while deacetylase inhibition alone caused only a small increase of TDP-43-containing droplets in neuron-like SHSY-5Y cells, both the numbers and diameters of these shells were enhanced by transient, partial inhibition of proteasome activity (by addition of the FDA-approved bortezomib (BTZ) for 4 hours) (Fig. 1I). Such de-mixing of wildtype TDP-43 did not require elevating its expression. Wildtype TDP-43 expressed from endogenous alleles de-mixed into spherical shells upon deacetylase and proteasome inhibition in induced pluripotent stem cell (iPSC)-derived human motor neurons (Fig. 1J), results indicating that TDP-43 naturally undergoes acetylation and deacetylation in these neurons.

## Anisosomes – TDP-43 liquid spherical shells with liquid crystalline properties

Liquid crystals flow like a conventional liquid but contain non-randomly oriented molecules producing a birefringent, anisotropic liquid (43). Complete extinction microscopy with a

pair of polarizers perpendicular to each other (Figs. 2A and 2B), conditions in which image brightness correlates with the level of anisotropy (44), was used to determine that the shells (but not cores) of RNA-binding deficient TDP-43 droplets were the only non-membrane component visible, indicating anisotropic subdomains (Fig. 2C, and Movie S3). Live imaging provided further evidence of the liquid properties of the shells, with the positions of the ordered subdomains changing faster than our (180 ms) detection limit (Fig. 2C). As expected, lipid bilayers of all cellular membrane compartments, another biological liquid crystal (45), were also visible, while de-mixed nucleoli (26) were not distinguished from surrounding nucleoplasm (Figs. 2D and 2E). Because of the uneven distribution of TDP-43 in these droplets, and their anisotropic property, we propose to name these intranuclear TDP-43 droplets "anisosomes" from the Greek "ánisos" and "soma", meaning "uneven body".

Anisotropy of ordered biomacromolecules changes or disappears as temperature increases (46, 47) because increased entropy changes the interaction between the biomacromolecules that mediate the anisotropic alignment. Consequently, we performed live DIC imaging during temperature increase from 37 to 39 °C (Figs. S2A to S2F, and Movie S4). Anisosomes gradually transformed into uniform liquid droplets (Fig. S2D) which fused and changed shape over time (Fig. S2E). Uniform oval droplets reconverted into anisosomes as the temperature was reduced to 37°C (Fig. S2F). Heat shock (20 minutes at 42 °C) also transformed anisosomes into uniform droplets (Fig. S2G).

## RNA-binding deficient TDP-43 recruits wildtype TDP-43

Next, we tested if RNA-binding deficient TDP-43 recruited wildtype TDP-43 to phase separate into shells and cores of anisosomes. We started with a cell line (10) in which endogenously expressed TDP-43 was replaced with a fluorescently-tagged wildtype TDP-43 (hereafter TDP-43[WT-mRuby]), with TDP-43 autoregulation (5, 48) maintaining normal TDP-43 level (Figs. S3A and S3B). We then introduced RNA-binding deficient TDP-43 variants, which as expected de-mixed into anisosomes and recruited TDP-43[WT-mRuby] (Fig. S3C). Over an 18-hour course, TDP-43[WT-mRuby] was recruited with RNA-binding deficient TDP-43[5FL-clover] into anisosomes (Figs. S3D and S3E). Use of FRAP to bleach either the RNA-binding deficient mutant TDP-43[5FL-clover] or TDP-43[WT-mRuby] within half of a nucleus revealed comparably rapid kinetics of recovery of red and green fluorescence within both shells and cores of individual bleached droplets, with corresponding fluorescence losses from unbleached droplets (Figs. S3F and S3G). Thus, RNA-binding deficient TDP-43 effectively recruits wildtype TDP-43 into the anisosomes.

## TDP-43 anisosomes are densely packed membraneless compartments

Conventional transmission electron microscopy (TEM) revealed that despite the liquid character of anisosomal shells and cores, the liquid shells were easily visualized (with a standard $OsO_4$ staining protocol) following induction of RNA-binding deficient TDP-43[2KQ], but not TDP-43[WT] (Figs. 3A to 3C). Cross sections of TDP-43 anisosomes were close-to-perfect annuli of diameters between 0.5 and 2 μm (Fig. 3C and S4). Distribution of TDP-43[2KQ-clover] molecules across the shells was determined using 70~80nm ultrathin

sections of fixed cells incubated with gold particle-labeled GFP antibody that also recognizes clover. Antibody-bound gold particles were highly enriched in the shell, slightly enriched in the core, and very sparse in the nucleoplasm (Figs. 3D and S5). In contrast, TDP-43$^{WT-clover}$ formed droplets in which TDP-43 was uniformly distributed (Fig. 3D).

The average shell thickness was largely independent of the diameter of the anisosome (Figs. S4G to S4I). Some (~10%) anisosomal sections contained electron-lucent regions in the electron-dense shell, consistent with fusion events or a liquid phase exchanging between the inner droplet and the nucleoplasm (Fig. S4G). Use of TEM confirmed the temperature-dependent conversion from anisosomes to uniform droplets. Transient incubation at elevated temperature (20 minutes at 39°C) partially disrupted the shell structure, producing more irregular shapes, while at 42°C the shell disappeared, yielding uniform droplets of lighter electron density than anisosomes and which were still distinguished from the nucleoplasm (Figs. 3E and 3F).

The structure of anisosomes under physiological conditions in cells was determined with cryo-electron tomography (CryoET) (Fig. 3G). After creating thin lamellae (with cryo-FIB milling) (Fig. S6), tomographic reconstructions revealed that anisosomes had a well-defined annular ring of 320 nm ± 20 nm thickness, consisting of meshwork-like densities similar to the meshwork reported in tomographic images of in vitro reconstituted phase-separated compartments (49). Molecular density in the anisosomal core appeared lower than in adjacent nucleoplasm (Fig. 3H). The tomograms revealed that anisosomal structure was consistent with a liquid center surrounded by a porous, meshwork-like rim through which some molecules can shuttle.

## Reduced proteasome activity drives anisosome formation within neurons in vivo

Recognizing that proteosome activity in the mammalian nervous system declines with age (33), we used peripheral injection of the proteasome inhibitor BTZ to reduce its activity within rat dorsal root ganglion neurons (DRG). This produced easily observable intranuclear annular structures (0.2 – 1 μm in diameter), whose shells were enriched in endogenous, wildtype TDP-43 (as determined using immunogold electron microscopy - Figs. 4A to 4C).

While nuclear aggregates, but not anisosomes, of TDP-43 have been repeatedly reported in postmortem samples of FTD and AD patients (8, 9), we tested if TDP-43-containing anisosomes would be maintained following the delays inherent in sample collection for human postmortem analyses. Following peripheral injection of a proteasome inhibitor, DRGs were collected freshly or after a 2-hour postmortem interval sufficient for ATP depletion (Fig. 4D). Electron microscopic analyses of the DRGs revealed that the freshly perfused samples preserved anisosomal structure (Fig. 4E), while as short as a 2-hour postmortem delay (during which rigor mortis initiated from depleted ATP levels) yielded complete loss of anisosomes and their replacement with nuclear aggregates (Fig. 4F).

## TDP-43 anisosomes are a selective barrier to some intranuclear components

Examination of anisosomal shells from RNA-binding deficient TDP-43 revealed the exclusion of several intranuclear components, including chromatin (marked by histone H2B - Fig. 5A), behavior similar to that previously reported for LLPS of artificial nuclear proteins and consistent with exclusion mediated by surface tension (50). Also excluded were some RNA-binding proteins, including FUS (mutations in which cause ALS) and iavNP, an RNA-binding protein encoded by the human influenza A virus (Fig. 5B). Other RNA-binding proteins (hnRNPA2B1, hnRNPH1 and hnRNPK), however, freely diffused into both the shell and core (Fig. 5C). Nuclear-targeted GFP (51) also freely diffused across the shell (Fig. 5B). Recognizing that anisosomes contained both RNA-binding deficient and wildtype TDP-43, as well as other RNA-binding proteins, we then determined RNA content by using CLICK-chemistry to fluorescently label RNA after incorporation of 5-ethynyl uridine (5-eU) (Fig. 5D). Imaging of individual anisosomes and surrounding nucleoplasm revealed that RNA was depleted from shells and cores relative to nucleoplasm (Figs. 5E and 5F).

Remarkably, intranuclear anisosomes remained intact after exposure to the cytoplasm during mitosis (Fig. 5G) and were then excluded from newly forming post-mitotic nuclei in earliest interphase (Figs. 5G and 5H). RNA-binding deficient TDP-43[2KQ] was likely re-imported into daughter nuclei and reassembled into anisosomes within 2 hours after mitotic exit, as the size of cytoplasmic droplets decreased quickly within 10 minutes (see droplets #1–7, Fig. 5H). Anisosomes also formed in micronuclei produced by chromosome missegregation and there was an increase of total number of anisosomes within the two daughter nuclei, as expected from TDP-43 re-importation through nuclear pores (Fig. 5H).

## Oligomerization and prion-like domains of TDP-43 are required for anisosome formation

To identify the interactions that maintain anisosomal structure, we first determined that forcing RNA-binding deficient TDP-43 to accumulate in the cytoplasm (by mutation of the nuclear localization sequence) largely eliminated anisosomes (Figs. S7A and S7B). TDP-43 possesses an N-terminal self-interaction domain (NTD) (34) that mediates its oligomerization (Figs. S7C and S7D) through three intermolecular salt bridges (34, 35). Disrupting self-interaction [by converting serine 48 in one bridge to a phosphorylation mimicking residue (glutamic acid) or by mutating glycine 53 to aspartic acid that is part of forming a second bridge (Figs. S7E and S7F)] completely disrupted anisosomal formation of TDP-43. The NTD alone did not form intranuclear droplets or anisosomes. However, it was sufficient to drive intranuclear phase separation into droplets, but not anisosomes, when linked to LCD domains from FUS or EWS (Figs. S7G and S7H), other RNA-binding proteins previously shown to be able to phase separate (52).

TDP-43 is the only hnRNP that contains a folded, self-interacting N-terminal domain, which is likely to enable its phase separation into anisotropic droplets. Indeed, while many efforts have focused on how phase separation is mediated by LCDs, single amino acid changes in

its amino terminus are sufficient to block anisosomes assembled from RNA-binding deficient TDP-43 (Figs. S7E and S7F), consistent with self-interaction of the N-terminal domain mediated by salt bridges formed by residues Gly53 and Ser48 of one unit with Glu17 of the neighboring unit (34). A disease-causing mutation (G335D) that partially disrupts the helices formed by the conserved region in the LCD of TDP-43 (53) did not affect anisosomal structure (Fig. S7I). Similarly, anisosomal structure was not affected by a corresponding variant (G335A) that decreased the dynamics of de-mixed LCD droplets in vitro (Fig. S7J) (53).

## Modeling predicts a low affinity TDP-43 partner in the anisosomal core

To identify mechanisms that can drive anisosomal formation, we created a mathematical model of an RNA-binding deficient TDP-43 in the presence of RNA (as it would be in a cell). Because the majority of TDP-43 molecules form stable dimers or even oligomers in vitro (35, 54) and perhaps in vivo *(34, 55)* and because nuclei have a high RNA concentration (Figs. 5F and S8), we modeled a de-mixing system which included RNA and monomers and dimers of the acetylation-mimicking TDP-43$^{2KQ}$, neither of which have affinity for the RNA (Fig. 6A). We employed a Cahn Hilliard diffuse interface model coupled with a Flory Huggins free energy scheme that employs the parameter $\chi$ to describe the energetic favorability of different components mixing in the system. Each pair of solute species had a parameter $\chi$ representing their energy cost of mixing. Higher values of $\chi$ represented a larger energy cost, favoring de-mixing. In this model, two TDP-43$^{2KQ}$ monomers (P) came together to form the TDP-43 dimer (P$_2$). We further assumed that once formed, it was energetically unfavorable for the dimer (P$_2$) to mix with both the nucleoplasm and the RNA. Conversely, RNA was diffusely distributed throughout nucleoplasm. With this modeling structure, TDP-43$^{2KQ}$ monomers formed dimers (P$_2$) which then rapidly de-mixed from the RNA-containing nucleoplasm forming only uniform droplets, not spherical shells (Fig. S8D).

Because a simple mixture of acetylated TDP-43 and RNA failed to form anisosomes in our initial model, we extended it to include a hypothetical entity, Y, representing one or more proteins that possessed both self-interaction and propensity to de-mix with TDP-43$^{2KQ}$ dimer. This approach built upon prior modeling work in which two components from a surrounding solution de-mixed into the same droplet, with one occupying the spherical core and the other forming a shell between the droplet core and the diffuse phase (56). Binding interaction energies and initial conditions were sampled to determine conditions that favored annuli formation. In particular, annuli formation was sensitive to the initial ratio between Y and the TDP43 monomer, as well as the ratio of the binding interaction kinetics for TDP43 dimer formation. However, there was a robust range of parameter values that allow for this phenomenon to occur. Upon introducing this hypothetical Y protein into the model, shell de-mixing was induced, but only when TDP-43 dimer bound Y with an intermediate affinity (Figs. 6B and S9).

Further, because RNA was reduced inside the TDP-43 anisosomes (Fig. 5D), we also hypothesized that it was energetically unfavorable for Y to mix with the diffuse RNA. Introduction of Y into a mixture of TDP-43$^{2KQ}$ and RNA successfully modeled de-mixing

of TDP-43 into anisosome-like structures, with Y forming the core (Fig. 6B) and a predicted volume fraction of TDP-43 in the shell about two times that of the inner droplet (Fig. 6C). The model closely predicted the actual 2.3–2.9 fold experimentally measured ratio of TDP-43 in anisosomal shells and cores formed with TDP-43$^{2KQ\text{-}clover}$, as determined by fluorescence intensity from optical slices (Figs. 6D to 6F) or immunogold electron microscopy (Figs. 6G and 6H).

## HSP70 family chaperones enrich in the liquid core of TDP-43 anisosomes

Because introduction of the unknown Y component allowed anisosome formation in our model, a proteomic approach was undertaken to determine the identity(ies) of such components in the liquid cores of TDP-43 anisosomes. A combination of differential isotope labeling of cells with or without TDP-43 anisosomes was coupled with proximity labeling (with biotin) of proteins close to peroxidase tagged TDP-43 (Fig. S10A), followed by immunoprecipitation and quantitative mass spectrometry (Fig. 7A). When stably expressed, TDP-43$^{mRuby2\text{-}APEX}$, a wildtype TDP-43 fused to red fluorescent protein (mRuby2) and peroxidase (APEX2) tags, accumulated intranuclearly with a proportion de-mixed into droplets (Fig. S10B). Induction TDP-43$^{2KQ\text{-}clover}$ yielded co-de-mixing of the RNA-binding competent and incompetent TDP-43's into abundant anisosomes (Fig. S10B).

Cells were isotope-labeled in the absence or presence of anisosomes and briefly exposed to H$_2$O$_2$ to enable APEX2 to label proximal proteins with biotin. Quantitative mass spectrometry was used to identify that only proteins enriched at least 6-fold in TDP-43 anisosomes were the five members of the HSP70 family of ATP-dependent protein folding chaperones (HSPA1A, HSPA1L, HSPA5, HSPA6, and HSPA8), with each enriched between 6- and 16-fold (Fig. 7B). We determined that indirect immunofluorescence could not be used to determine content of the cores because conventional fixation produces a barrier of crosslinked shell proteins that prevents antibody penetration to the core (Fig. S11). Correspondingly, expression of mRuby2 tagged HSPA1A, HSPA1L, HSPA6 or HSPA8 was used to validate that each of these HSP70 family members was indeed enriched in the anisosomal cores (Fig. 7C).

## ATP-dependent HSP70 chaperone activity maintains the anisosomal structure

Our mathematical modeling also predicted that anisosomal shells convert into uniformly phase separated droplets when the affinity between "Y" (HSP70) and TDP-43$^{2KQ}$ is increased (Fig. S12). We found that shells enriched in TDP-43 rapidly (and reversibly) merged with their liquid cores (Fig. S2) when the HSP70 association with TDP-43 was enhanced by mild temperature increase (57). Each HSP70 family member requires ATP hydrolysis to fulfill its protein-folding chaperone function (58). After addition of an HSP70 inhibitor thought to block ATP hydrolysis by all family members (59) and to lock the chaperone onto a client protein (58), TDP-43$^{2KQ}$ anisosomes converted within 10 minutes into small droplets of uniformly distributed TDP-43$^{2KQ}$ and HSP70. In an additional 30–60 minutes, these droplets fused into a single large particle, whose formation was reversible, with anisosomes reforming within 6 minutes after removal of the HSP70 inhibitor (Figs. 8A

and 8D). HSP70 molecules in the liquid anisosomal cores were highly dynamic, quickly recovering ($t_{1/2}$ = 3 sec) after photobleaching (Figs. 8C and 8D). After HSP70 inhibition, however, TDP-43$^{2KQ\text{-}clover}$ anisosomes converted into an intranuclear gel (with little recovery after photobleaching), while HSP70 in the particles retained liquid character, albeit with much slower ($t_{1/2}$ = 50 sec) recovery after photobleaching. Importantly, transient depletion of ATP by blocking mitochondrial ATP synthesis and glucose starvation also caused anisosomes to collapse (Fig. S13). Intracellular HSP70 interaction with TDP-43 was determined to be mediated primarily through its RRMs, with enhanced interaction with RNA-binding deficient TDP-43 (Fig. S14). HSP70 did not form intranuclear membraneless condensates by itself (Fig. 7C) or in the absence of TDP-43 (Fig. S15). Thus, we found no evidence of pre-existing liquid cores around which RNA-binding deficient TDP-43 condensed to form anisosomes.

Cytoplasmic TDP-43 aggregation has been observed in many age-related neurodegenerative diseases (1–4). The known reduction in nuclear/cytoplasmic transport during aging of the mammalian nervous system (10, 60) would facilitate an age-dependent increase in cytoplasmic TDP-43. Recognizing this, and that HSP70 accumulates to a high level in the cytoplasm (Fig. 7C), we tested how reducing HSP70 chaperone activity affected cytoplasmic TDP-43 behavior following removal of its NLS to mimic age-dependent reduction in TDP-43 nuclear import (Fig. 8E). Within 1 hour after addition of the HSP70 inhibitor, cytoplasmic RNA-binding deficient TDP-43 converted from diffusely localized, soluble TDP-43 into round cytoplasmic droplets whose number and diameter increased with time (Figs. 8F). Further, use of photobleaching revealed that initially liquid droplets converted into gel/solids, as indicated by slow, very partial fluorescence recovery after photobleaching (Fig. 8G).

## Discussion

Here we report that ALS-causing mutations, acetylation-mimicking mutations, or increased acetylation of wildtype TDP-43 - each of which reduces its RNA-binding - drove phase separation with RNA-binding competent TDP-43 into droplets comprised of an anisotropic, liquid spherical shell enriched in TDP-43 and a liquid core comprised of HSP70 family chaperones (as well as TDP-43), structures which we termed TDP-43 anisosomes. Liquidity of both shells and cores was dependent on continuing ATPase-dependent chaperone activity. Unlike previously identified intracellular liquid droplets, including the nucleolus (24), anisosomal cores were centrally aligned so as to produce symmetrical liquid shells. Cryo-electron tomography, traditional EM, and fluorescence microscopy of TDP-43 intranuclear anisosomes revealed the exclusion of chromatin and some RNA-binding proteins, while other RNA-binding proteins freely exchanged, as demonstrated with photobleaching. TDP-43 anisosomes exhibited birefringence, evidence that an anisotropic liquid could be formed intracellularly by protein phase separation in complex nucleoplasm. While acetylation of histones H1 and H3 has recently been reported to abolish liquid-liquid phase separation of chromatin (61), acetylation of TDP-43 did the opposite: it promoted phase separation. Recognizing that protein acetyltransferases are enriched in transcription initiation complexes (40), phase separation of TDP-43 near sites of transcription could form

a barrier to include some but exclude other RNA-binding proteins, as a means to facilitate pre-mRNA maturation.

Our modeling strongly supported an essential role for the HSP70 family of chaperones in anisosome formation, as continuing chaperone activity was required for generation and maintenance of the liquidity of the shells and cores. Indeed, depletion of ATP induced anisosome collapse and conversion into aggregates of TDP-43 in cultured cells and in neurons of the murine nervous system following post mortem ATP depletion, the latter producing images consistent with what has been reported for wildtype TDP-43 in familial and sporadic FTD (6, 7). Loss of RNA-binding would be expected to expose one or more unstable interfaces within TDP-43's RRM domains including hydrophobic residues that mediate protein-RNA interaction (62) and whose exposure to nucleoplasm would recruit, and be stabilized by, HSP70 chaperone activity. While HSP70's activity in the cytoplasm has been reported to be required to disassemble stress granules (63), its role in facilitating anisosome formation and maintenance adds an additional role for nuclear HSP70, which has been reported to facilitate delivery of aggregation-prone proteins to the nucleolus for proteasomal degradation during heat shock (64).

The TDP-43 anisosome was different from reentrant phase separation (RPS), a phenomenon identified in vitro using two purified components and in which moderate concentrations of a charged polymer (e.g., RNA) drive assembly of hollow droplets of an oppositely charged polymer (e.g., a positively charged polypeptide), with the thickness of the shell changing in a concentration-dependent manner and superstoichiometric concentrations driving droplet disassembly (65, 66). TDP-43 anisosomes, on the other hand, were formed from RNA-free TDP-43 and the ATP-dependent chaperone action of HSP70 variants.

Spherical shells similar to TDP-43 anisosomes have been reported in Drosophila germ granules, first reported as intranuclear spherical shells (67) and later shown to be gel-like (68). Furthermore, annular nuclear bodies, apparently containing both polyA-RNA and the RNA-binding protein SAM68, have also been reported (69) in degenerating motor neurons of SMN 7 mice, a model of spinal muscular atrophy type II. Matrin3, a protein encoded by an ALS-causing gene (70), forms round and apparently hollow nuclear droplets when its second RNA-binding domain is removed, albeit it has not been tested if these droplets have liquid properties.

Abnormal aggregation of TDP-43 is nearly a universal feature in ALS and in FTD with ubiquitin positive inclusions (FTLD-U) (71, 72), in hippocampal neurons of Alzheimer's disease [where it is correlated with ApoE4 alleles] (73–75), and in LATE, a dementia in the oldest individuals (4). TDP-43 aggregates have been reported in both the nucleus and the cytoplasm of neurons in postmortem FTD and AD nervous system tissues (8, 9). ALS and FTD-causing TDP-43 mutants (such as P112H, K181E and K263E) have diminished RNA-binding and form anisosomes in cells. Where examined, acetylated, RNA-binding deficient TDP-43 is present in pathological TDP-43 aggregates (16). Here we have shown that TDP-43-containing anisosomes could be driven simply by altering the balance of ongoing acetylation/deacetylation or in neurons of the mammalian nervous system experiencing proteomic stress from transient proteasome inhibition. Added to this, we have shown here

that when ATP levels declined, as they did during the postmortem interval required for typical human nervous system tissue collection, TDP-43 anisosomes converted into aggregates. Altogether, the evidence suggests that anisosomes may be precursors of nuclear and/or cytoplasmic TDP-43 aggregates found in FTD, AD, LATE, and ALS (7–9, 36, 37).

Finally, our results have suggested an essential partnership between TDP-43 and HSP70 chaperones in driving and maintaining TDP-43 phase separation and preventing TDP-43 aggregation. Future efforts are now needed to determine the identities of the TDP-43 acetylases and deacetylases that act on TDP-43 and whether there are age-dependent changes in their activities that may synergize with the known age-dependent or drug-induced decline in proteasome (32, 33) and nuclear import (60) activities to mediate stress-induced TDP-43 phase separation in age-related neurodegeneration (4, 6, 8, 9, 36, 37, 71–75) and chemotherapy-induced peripheral neuropathy (76–78).

## Materials and Methods

### Plasmids

The information on all plasmids used in this paper is listed in Supplementary Table S1. In brief, the entry vectors (pHY135 and pHY195) were used as backbones for most of the lentiviral vectors, generated by traditional cloning method (using double-restriction digestion followed by ligation) or Gibson assembly (79). All plasmids in this manuscript will be deposited to Addgene. TDP-43$^{2KQ}$, and TDP-43$^{mNLS,2KQ}$ cDNA was a gift from Dr. Todd Cohen. All other TDP-43 variants were constructed by H.Y. with the help of D. T., S. L., and S.V.S.

### Cell culture, siRNA-knockdown, transient transfection and lentiviral transduction

Cell lines used in this paper are: HEK293T (ATCC: CRL-11268), U2OS (ATCC: HTB-96), SH-SY5Y (ATCC: CRL-2266), human iPS cell line CV-C – a gift from Eugene Yeo's group at UCSD (maintenance and differentiation will be described in a different section), and TDP-43 knockout HEK293T cells – a gift from Dr. Broder Schmidt (80). Routine maintenance of these model cell lines follows the standard protocol. In brief, U2OS and HEK293T cells were cultured in complete DMEM supplemented with 10% Fetal bovine serum (FBS). SH-SY5Y cells were cultured in DMEM/F12 supplemented with 10% FBS. HEK293T (TDP-43$^{KO}$) cell line (80) were cultured in DMEM supplemented with NEAA (Gibco, 11140050, 100X), Sodium Pyruvate (Gibco, 11360070, 100X) and 10% FBS.

Transient transfection was performed for HEK293T cells and U2OS cells at 60% confluency, by using transfection reagent TransIT X2 (Mirus, MIR6000) and the standard protocol posted on the product page of TransIT X2. In brief, serum free DMEM was used to dissolve DNA, and then TransIT X2 was added to the mix. After 15 minutes, the final mix was added dropwise to attached cells. The culture medium was changed after 12~24 hours post transfection.

To package lentivirus, a second-generation packaging system was used. Briefly, 0.5 million 293T cells were seeded per well in a 6-well plate. For lentiviral transfection, 2.5 μg of the lentiviral plasmid, 1.25 μg of pMD2.G and 0.625 μg of psPAX2 were inoculated to each well

using the transIT-X2 transfection reagent. Culture medium was changed to fresh medium at 12~24 hours post transfection. Two days after transfection, the culture medium was filtered through a 0.45 μm syringe filter to generate the viral stock. 10–50 μg/mL protamine sulfate was added to the viral stock for transduction of U2OS or SH-SY5Y cells. After 24 hours of incubation with cells, the virus-containing media were removed and cells were passaged once before selection. Transduced cells are selected based on the selection marker encoded by the lentivirus. For U2OS, the concentrations of the antibiotics used for selection were 200 μg/mL for neomycin (G418, Gibco 10131035), 20 μg/mL for blasticidin (Gibco A1113903), and 1 μg/mL for puromycin (Gibco A1113803). For SH-SY5Y cells, the concentrations were 400 μg/mL for neomycin, 10 μg/mL for blasticidin and 3 μg/mL for puromycin. Detailed guides and protocols posted can be found on the Addgene website:

https://www.addgene.org/protocols/lentivirus-production/

https://www.addgene.org/guides/lentivirus/

The siRNA experiment used the same protocol and reagents as previously described by Melamed *et al* (13).

### Human induced pluripotent stem cell (iPSC) culture

Human iPSCs were grown in Matrigel-coated dishes (Corning, 354234) and mTeSR Plus media (StemCell Technologies, 05825) and passaged using Accutase (Innovative Cell Technologies, Inc., AT-104). ROCK inhibitor Y27632 (ApexBio, B1293–10) was used at 10μM for 24h after every passaging or thawing.

### Motor neuron differentiation from human iPSCs

The iPSCs were differentiated according to a modified version of Martinez *et al.* (81), based on the established strategy of dual-SMAD inhibition (82, 83). iPSC dishes at 60–80% confluency were placed in 0.5XN2B27 media (DMEM/F12 + GlutaMAX media (Life Technologies, 10565–018) supplemented with 0.5X N2 supplement (Life Technologies, 17502–048), 0.5X B27 supplement (Life Technologies, 17504–044), 0.1 mM Ascorbic Acid (Sigma-Aldrich, A4544), and 1% PenStrep (Life Technologies, 15140–122)), which was supplemented with the different compounds throughout differentiation. On days 1–6, cells were fed daily with 0.5XN2B27 media in the presence of 1 μM Dorsomorphin (Tocris, 3093), 10 μM SB431542 (Tocris, 1614) and 3 μM CHIR99021 (Tocris, 4423). On day 7–18, cells were fed daily with 0.5X N2B27 in the presence of 1 μM Dorsomorphin, 10 μM SB431542, 0.2 μM Smoothened Agonist (SAG) (EMD Biosciences, 566660) and 1.5 μM Retinoic Acid (Sigma-Aldrich, R2625). On days 18–21, cells were fed every other day with 0.5XN2B27 in the presence of 0.2 μM SAG and 1.5 μM Retinoic Acid. On day 22 cells were passaged onto poly-Ornithine (Sigma-Aldrich, P3655) / poly-D-Lysine (Sigma-Aldrich, P6407) / Laminin (Sigma-Aldrich, L2020) coated plates, and on days 22–25 were fed with 0.5XN2B27 supplemented with 2 ng/μl of BDNF (R&D Systems, 248-BD), CTNF (R&D Systems, 257NT) and GDNF (R&D Systems, 212GD), in the presence of 2 μM DAPT (Tocris, 2634). From days 25 on, cells are fed every 2–3 days with 0.5XN2B27 supplemented with 2 ng/μl of BDNF, CTNF and GDNF. Cells were treated with 5 μM Ara-C (Sigma-Aldrich, C1768) for 48h to avoid expansion of glial cells.

## Fluorescence activated cell sorting (FACS)

Before cell sorting or flowcytometry analysis, cells were trypsinized and resuspended in FACS buffer (1% FBS in PBS). Cell suspension was passed 40 μm strainer (Corning #352235) to form single cell suspension. The cells were loaded to SONY SH800S cell sorter to sort for single cell clones, or a population of defined clover fluorescence. For flowcytometry analyses, BD LSR-Fortessa was used.

## Chemical treatments

Doxycycline (DOX Sigma-Aldrich, D9891) was used to induce gene expression via the TetON3G promoter. U2OS cell and SH-SY5Y cells were treated at 500ng/mL final concentration of DOX. Trichostatin A (TSA, ApexBio, A8183) at 10 μg/mL and Vorinostat (SAHA, ApexBio, A4084) at 20 μM final concentrations were used to inhibit HDAC activity in HEK293T, U2OS and SH-SY5Y cells. Bortezomib (BTZ, ApexBio, A2614) at 2.5 μM final concentration was used to inhibit the proteasome function in SH-SY5Y cells and iPSC-derived motor neurons. RNA labeling was conducted by following the protocol of the kit (Thermo-Fisher, C10330). HSP70 inhibitor (VER155008, ApexBio, A4387) was used at 50 μM final concentration. To inhibit ATP production from mitochondria, 1 μM antimycin (Sigma-Aldrich, A8674) with 1 μM oligomycin (Sigma-Aldrich, O4876) (84) or 10mM sodium azide (Sigma-Aldrich, S2002) (85) was used.

## Fluorescence microscopy

Immunostaining and fluorescence images were acquired using a Zeiss LSM880 confocal microscope with Airyscan or a Leica SP8 confocal microscope with lightening deconvolution. Before imaging, cells were seeded in glass-bottom 8-well μ-slide (iBidi 80827). For live cell imaging, cells were incubated in Leibovitz's L-15 Medium supplemented with 10% FBS. For immunofluorescence, cells were first fixed with 4% PFA for 10 minutes at room temperature (RT), washed twice with PBS, and permeabilized by using 0.5% Triton X-100 in PBS. Then cells were incubated with blocking buffer (2% BSA, 0.1% Triton X-100 in PBS) for 30 minutes at RT. Primary antibodies were diluted in the blocking buffer, and cells were incubated with primary antibody over night at 4°C. Then cells were washed 3 times at RT by the washing buffer (0.1% Triton X-100 in PBS). Cells were incubated with secondary antibodies diluted in blocking buffer for 45 minutes at RT, covered from light. After the incubation with secondary antibodies, cells were washed 4 times at RT with washing buffer and stained with DAPI (Tocris #5748) at 1 μg/mL in PBS. After DAPI staining, cells were post-fixed by 4% PFA for 5 minutes at RT, and washed with PBS twice afterward, to immobilize the antibodies on their antigens. Then cells were mounted with ProLong Gold (Thermo-Fisher P10144) and 8mm coverslips (Electron Microscopy Sciences #72296–08).

## Differential interference contrast (DIC) microscopy and complete extinction microscopy (CEM)

Both DIC and CEM were performed by using Nikon Eclipse Ti2-E microscope, equipped with 100x lens, TC-C-DICP-I intelligent linear polarizer (adjustable), a build-in linear polarizer in the base unit, $CO_2$ and temperature was maintained by Okolab H101 water

jacket stage top chamber with lens heater, Okolab CO2 unit, and Oko-touch digital recorder. The sample temperature was recorded every 30s during the experiment. For DIC microscopy, the Nomarski prism was inserted to the base of the lens, and the adjustable polarizer was turned to obtain optimal contrast. For CEM, the Nomarski prism was pulled out (this is a critical step because the Nomarski prism generates artifact), and the microscope was set to a position where only two polarizers are in the light pass. Images and movies were taken when the two linear polarizers are aligned at 0°, which allows maximum amount of light to pass. Then the adjustable linear polarizer was turned to a position where the least amount of light was detected by the camera. This position was defined as the complete extinction position.

### Fluorescence recovery after photobleaching (FRAP) analysis and quantification

FRAP experiments on U2OS cells were performed on Zeiss LSM880 Airyscan microscope with 40x/1.2 Water objective at 37°C. The intensity of the fluorescent signal is controlled in the detection range through changing the laser power, digital gain and off-set. For the green channel, bleaching was conducted by a 488 nm line from an argon laser at ~80%−100% intensity with ~10–20 iterations. Fluorescence recovery was monitored at 2 seconds, 5 seconds or 10 seconds intervals for 3 minutes. In the focal-bleach experiment, roughly half of a particle is bleached, and then the distribution of the fluorescence within the bleached particle is determined over time. During the experiment cells were maintained in Leibovitz's L-15 medium (CO2 independent).

The FRAP data was quantified using Image J. The time series of the granule fluorescence intensity was calculated and the intensity of the background (area with no cells) was subtracted from the granule intensity. The intensity of the granule during the whole experiment was normalized to 1 before bleaching. An average of at least 10~20 particles per condition was used to calculate the mean and standard error. The averaged relative intensity and standard error were plotted to calculate the dynamics of the particles.

### Immunoblotting

Sample collection: Cells were washed by ice cold PBS on ice before lysis using RIPA buffer. To remove DNA and RNA, and inhibit protease activity, RIPA buffer were supplemented with benzonase (Millipore, 101654) at 1 U/mL and protease inhibitor cocktail at 1X (100X cocktail from Thermo-Fisher, 78430). Cells were lysed with 200 μL per well for 6-well plate for 20 minutes and collected in 1.5 mL tubes. Lysates were centrifuged at 15000 g for 10 minutes. Supernatant were mixed with NuPAGE LDS sample buffer (Thermo-Fisher, NP0007). All procedures were performed on ice or at 4 °C before boiling for 10 minutes at 95 °C. SDS page, transfer, and blotting procedures were performed by following standard protocol. ECL substrates were used to visualize HRP-conjugated secondary antibody on the blot, and Biorad ChemiDoc system was used to capture the luminescent signals.

### Co-Immunoprecipitation (co-IP)

HEK293T cells stably expressing HSPA1A$^{mRuby2-Flag}$ were induced to express TDP-43 variants (clover-tagged). After 2 days induction, cells were lysed with RIPA supplemented with protease inhibitors and 2 mM DTT. For some conditions, the lysis buffer was

supplemented with 5 mM ATP. Cell lysate was then sonicated for 2 seconds at 35% amplitude for 2 times to shear the genomic DNA. Debris was pelleted by 10-minute centrifugation at 20000g at 4 °C. Anti-Flag M2 affinity gel (Sigma-Aldrich, A2220) was washed twice with complete RIPA buffer. To perform the co-IP experiment, 90% of the supernatant was added to 50 μL affinity gel and incubated at 4 °C for 1 hour. Then, the supernatant was removed, and the gel was washed 3 times with complete RIPA buffer at 4 °C. The protein on the gel was released by adding 2 x Laemmli SDS sample buffer and boiling for 10 minutes for immunoblotting. To eliminate the background of IgG heavy chain, anti-mouse light chain secondary antibody (Jackson Immunology #115–035-174) was used for immunoblotting.

### Laboratory animals

Sprague-Dawley rats at five weeks of age and C57BL/6J mice at four months of age (The Jackson Laboratory, stock# 000664) were used for intravenous injection of BTZ (0.5mg/kg). Rat care, handling and experimental procedures were in accordance with Spanish legislation and the guidelines of the European Commission for the accommodation and care of laboratory animals. The experimental plan was preliminarily examined and approved by the Ethics Committee of the University of Cantabria. Mouse care, handling and experimental procedures were approved by the Institutional Animal Care and Use Committee of the University of California, San Diego. All the animals were housed in a limited access environment with a 12-h light/dark cycle, where room temperature and relative humidity were set at $22 \pm 2$ °C and $55 \pm 10\%$ respectively and there was free access to food and water. Animal sacrifice was performed under deep pentobarbital anesthesia (50 mg/kg) or in a euthanasia chamber containing 30% carbon dioxide.

### Electron microscopy (EM) and ImmunoEM

U2OS cells were plated on coverslips and induced by doxycycline to express TDP-43 variants. Cells were fixed by 2 % glutaraldehyde in 0.1 M sodium cacodylate (SC buffer) buffer for 60 minutes or longer at 4°C. After fixation, all procedures were carried out on ice. Fixed cells were washed with 0.1 M SC buffer five times and stained with 1% OsO4 in 0.1M SC buffer for 45 minutes. Stained cells were then washed with 0.1 M SC buffer five times and MilliQ water for 2 times. Coverslips were placed in 2% uranyl acetate buffer for 45 minutes and then rinsed with Milli-Q water. Samples were serial dehydrated by immersion during 1 minute in 20%, 50%, 70%, 90%, and two times in 100% ethanol and then two times in dry acetone. After dehydration, all steps were carried at room temperature (RT). Samples were then incubated with Ducurpan:Acetone = 50/50 for 1 hour, and then two times for 1 hour in fresh 100% Durcupan. Coverslips were embedded in Durcupan resin, and cut into 60nm ultrathin sections using a diamond knife. Sections were mounted on 300 mesh grids.

For immunoEM, U2OS cells containing TDP-43 anisosomes were fixed for 12h in 4% PFA in 0.1 M phosphate buffer, cryoprotected in sucrose, pelleted in 10% gelatin, and snap frozen in liquid nitrogen. Ultrathin cryosections (70–80 nm) were cut as previously described (Zheng et al., 2004). Sections were picked up with a 1:1 mixture of 2.3 M sucrose and 2% methyl cellulose (15cp) as described by Liou et al. (1996) and transferred onto Formvar and

carbon-coated copper grids. Immunolabeling was performed by a slight modification of the "Tokuyasu technique", (Tokuyasu, 1980). Briefly, grids were placed on 2% gelatin at 37 °C for 20 minutes, rinsed with 0.15 M glycine inPBS and the sections were blocked using 1% cold water fish-skin gelatin. For immunogold labeling of TDP-43[2KQ-clover], sections were sequentially incubated for 2h with a mouse anti-GFP antibody (Clontech Living Colors A.V. JL-8), followed by a 12nM gold conjugated goat anti-mouse IgG (Jackson Immunoresearch, 115–205-071) for 1h. Grids were then counterstained for 10 minutesin 0.4 % uranyl acetate and 1.8% methyl cellulose on ice.

For immunoEM of TDP-43 in rat tissue, bortezomib-treated rats were subjected to transcardial perfusion under deep anesthesia with 3.7 % paraformaldehyde in 0.1 M cacodylate buffer for 15 minutes at RT. Small tissue fragments of sensory ganglia were dissected and post-fixed in the same fixative solution for 4h at RT, washed in 0.1 M cacodylate buffer, dehydrated in increasing concentrations of methanol at −20 °C, embedded in Lowicryl K4M at −20 °C, and polymerized with ultraviolet irradiation. Ultrathin sections were mounted on Formvar coated nickel grids and sequentially incubated with 0.1 M glycine in PBS for 15 minutes, 3 % BSA in PBS for 30 minutes, and the primary rabbit polyclonal anti-TDP-43 antibody (diluted 1:100 in 50 mM Tris–HCl, pH 7.6, containing 1 % BSA and 0.1 M glycine) for 1 h at 37 °C. After washing, sections were incubated with the goat anti-rabbit IgG antibody coupled to 10-nm gold particles (BioCell, UK; diluted 1:50 in PBS containing 1 % BSA). Following immunogold labeling, the grids were stained with lead citrate and 2% (w/v) uranyl acetate. As controls, ultrathin sections were treated as described above but with the primary antibody being omitted.

Imaging was carried out using a JEOL 1200 EX II electron microscope equipped with an Orius CCD Gatan camera and Gatan digital micrograph software (Gatan, Pleasanton, CA; University of California, San Diego, Cellular and Molecular Medicine Electron Microscopy Facility).

The calculation of average thickness and outer diameter of anisosomes in EM images: For each cross section of anisosomes, the thickness was measured as the average of the 8 yellow lines an example is shown in panel S4G. The error bars are the SEM of the 8 values. The average outer diameter of an anisosome was measured by the average of the 2 red lines.

**Cryo-FIB milling and cryo-electron tomography**

U2OS cells were dox-induced for 2–6 days and then seeded on glow-discharged Quantifoil grids (R1/4, Au 200-mesh grid, Electron Microscopy Sciences). The cells were then cultured for 24 hrs with continued dox-induction. The grids were then manually blotted from the backside only (to remove excess media) and quickly plunge-frozen into liquid ethane/propane mixture using the custom-built vitrification device (Max Planck Institute for Biochemistry, Munich). From thereon, grids were always kept in cryogenic conditions. The grids were then clipped onto FIB-AutoGrids (ThermoFisher) for milling inside a Thermo Scientific Aquilos DualBeam. ~120–150 nm lamellae (~11 um in width) were prepared in the Aquilos using rectangular milling patterns as previously described[4,5]. Briefly, the coarse milling was performed with the ion beam current of 0.10–0.50 nA. The current was reduced to 10–50 pA for careful and slow fine milling.

The lamellae created on the grids were then stored in cryogenic conditions and eventually transferred to the transmission electron microscope (Titan Krios G3; ThermoFisher) using the AutoLoader (ThermoFisher). Tilt-images, in the form of cryo-transmission electron images, were acquired on the microscope operated at 300 kV and equipped with a Quantum post-column energy filter (Gatan). The images were recorded on a K2 Summit (Gatan) direct detector in the counting mode using the SerialEM software (86). The tilt-series acquisition parameters were as follows: tilt range: ± 60, magnification: 26000X-19500X, tilt increment: 3/2/1.5°, pixel size of 0.53–0.71 nm, target defocus: −5 μm. The images were recorded in the movie mode, the frames of the tilt-series images were motion corrected and dose-weighted using MotionCor2 (87). The tilt series were then aligned in IMOD using patch-tracking (88). No CTF correction was performed. The weighted back-projection method was used for the final tomographic reconstruction.

### Proximity labeling and enrichment of biotinylated protein

Before the labeling experiment, U2OS cells were passaged in (Lys0, Arg0) or heavy (Lys8, Arg10) DMEM medium for 5 generations. U2OS cells were incubated with 500 μM biotin phenol (Iris-Biotech, 41994–02-9) containing medium for 30 min. Then 1 mM hydrogen peroxide was added to the medium to activate APEX reaction for 1 min, followed by immediate quenching of reaction with ice-cold quenching buffer (1xPBS, 10 mM sodium azide, 10 mM sodium ascorbate, 5 mM Trolox). After washing with cold quenching buffer for three times, the cells were collected from plates with scrapers.

Cells were lysed in lysis buffer (100 mM NaPO4, PH 8.0, 8 M Urea, 0.05% SDS, 10 mM sodium azide, 10 mM sodium ascorbate, 5 mM Trolox supplemented with 500 unit benzonase to remove DNA and RNA) and rotated at room temperature for 15 minutes. Then SDS was increased to 1% and sonication was performed in a water bath sonicator for 10 minutes. Protein concentration was measured using 2-D quant kit (GE healthcare, 80648356), by following manufacturer' instructions. The denatured proteins were reduced with 5 mM TCEP and alkylated with 10 mM Iodoacetamide. Equal amount of proteins from light and heavy group were mixed together and then the mixed cell lysates were diluted with equal volume of ddH2O to reduce the concentration of urea to 4 M and SDS to 0.5 %. The samples were incubated with streptavidin magnetic beads at 4 °C overnight. After four washes with wash buffer (100 mM NaPO4, PH 8.0, 4 M Urea), the beads were resuspended in 100 mM TEAB, 2 M Urea supplemented with 10 ng/uL Trypsin, 5 ng/uL Lys-C for digestion overnight. The digested products were collected and added with 1% formic acid (final concentration) for LC-MS/MS analysis.

### Liquid chromatography-Mass spectrometry analysis

LC-MS/MS was conducted on Orbitrap Elite Hybrid Mass Spectrometer interfaced with a nano-flow HPLC Easy II. Digested peptides were loaded onto a 100 μm x 15 cm analytical column packed with 3 μm, 120 Å C18 resin (Phenomenex 04A-4758). The peptides were separated over a 90-minute linear gradient from 0% buffer B (95% acetonitrile, 0.1% formic acid), 100% buffer A (5% acetonitrile, 0.1% formic acid) to 30% buffer B, followed by a 10-minute gradient from 27% to 80% buffer B, then maintaining at 80% buffer B for 20 minutes. The flow rate was 300 nL/min. The MS parameters were: R = 140,000 in full scan,

R = 7,500 in HCD MS2 scan; the 10 most intense ions in each full scan were selected for HCD dissociation; the AGC targets were 1e6 for FTMS full scan and 5e4 for MS2; minimal signal threshold for MS2 was 5e3; precursors having a charge state of +1, or unassigned were excluded; normalized collision energy was set to 30; dynamic exclusion was on.

### Quantitative mass spectrometry data analysis

The raw data was processed by pParse (89), and co-eluting precursor ions were excluded. MS1 and MS2 data were searched using pFind 3 (90) against a complete human protein database downloaded from Uniprot with the addition of APEX2 and clover protein sequence. The settings of pFind 3 are: open search mode; 3 missed cleavage sites for trypsin digestion; peptide length 6–25 aa; fixed modification was carboxymethylation on Cys (58.0054 Da); variable modifications were oxidation on Met (15.9949 Da) and acetylation on N-term (42.0105 Da). The search results are filtered with less than 10 ppm mass deviation for precursor ions and 20 ppm for fragment ions, FDR < 0.01 at peptide level. The identified spectra were used for quantification with pQuant (91) with the setting of using 200 MS1 scans before and after the spectra corresponding to identified spectra for searching the chromatography peaks and allowing 2 holes in the chromatography peak and the intensity of ion within 10 ppm mass deviation was used.

The median value of the ratio of light to heavy peptides from each protein was used as the ratio of the protein. The ratios of each protein from two forward labeling groups and one reverse labeling group were used to calculate P-value through one sample t-test. The volcano plot was generated with R package.

### Mathematical Modeling

In building this model of TDP43 mutant phase separation, we initially considered whether the TDP43 mutant dimer could form annuli on its own by phase separating from the solvent and the RNA. While we observed exclusion of the RNA from the phase separated TDP43, we were unable to observe annuli formation by the TDP43 dimer, as shown in the Supplementary Material. Using our previous work (56), we knew that annulus-like pattern formation occurs when two components phase separate together, resulting in the proposal of Y. Further, when building this model to incorporate Y, four different sets of parameters needed to be considered: diffusion coefficients, $\chi$-values (de-mixing energy), binding rates, and initial conditions.

We used an established theoretical diffusion coefficient values for proteins, RNAs and the subsequent complexes they formed based on a comparison of their molecular weights (56). The code can be downloaded from this link: https://doi.og/10.5281/zenodo/4299457. We assumed, for simplicity, a lack of folding that would influence the diffusion coefficient. The molecular weight of the protein used in Gasior, Zhao et al (56) is similar to that of TDP-43, but the size of the RNA that can exist within the nucleus can vary drastically $10^2$-$10^5$). For simplicity, we used a value closer to the lower end of this range and thus modeled RNA to be 8x the molecular weight of the TDP-43 mutant, which is reflected in the diffusion coefficient. Further, because there are two monomers that are used to create the dimer, the TDP-43 mutant dimer has a diffusion coefficient half as large as the TDP43 mutant

monomer. The code can be downloaded from this link: https://doi.org/10.5281/zenodo.4287615.

## Statistics and data reproducibility

Except for the quantitative analyses for the proteomic data, student T-test (comparing two groups) and one-way ANOVA (comparing three groups or more) were used to calculate significance, and P<0.05 is considered statistically significant.

Each experiment was conducted at least three times or with at least three biological replicates.

## Supplementary Material

Refer to Web version on PubMed Central for supplementary material.

## Acknowledgments:

## References

1. Taylor JP, Brown RH Jr., Cleveland DW, Decoding ALS: from genes to mechanism. Nature 539, 197–206 (2016). [PubMed: 27830784]

2. Neumann M et al., Ubiquitinated TDP-43 in frontotemporal lobar degeneration and amyotrophic lateral sclerosis. Science 314, 130–133 (2006). [PubMed: 17023659]

3. Amador-Ortiz C et al., TDP-43 immunoreactivity in hippocampal sclerosis and Alzheimer's disease. Ann Neurol 61, 435–445 (2007). [PubMed: 17469117]

4. Nelson PT et al., Limbic-predominant age-related TDP-43 encephalopathy (LATE): consensus working group report. Brain 142, 1503–1527 (2019). [PubMed: 31039256]

5. Polymenidou M et al., Long pre-mRNA depletion and RNA missplicing contribute to neuronal vulnerability from loss of TDP-43. Nat Neurosci 14, 459–468 (2011). [PubMed: 21358643]

6. Mackenzie IR et al., A harmonized classification system for FTLD-TDP pathology. Acta Neuropathol 122, 111–113 (2011). [PubMed: 21644037]

7. Mackenzie IR, Neumann M, Reappraisal of TDP-43 pathology in FTLD-U subtypes. Acta Neuropathol 134, 79–96 (2017). [PubMed: 28466142]

8. Neumann M et al., TDP-43 in the ubiquitin pathology of frontotemporal dementia with VCP gene mutations. J Neuropathol Exp Neurol 66, 152–157 (2007). [PubMed: 17279000]

9. Tome SO et al., Distinct molecular patterns of TDP-43 pathology in Alzheimer's disease: relationship with clinical phenotypes. Acta Neuropathol Commun 8, 61 (2020). [PubMed: 32349792]

10. Gasset-Rosa F et al., Cytoplasmic TDP-43 De-mixing Independent of Stress Granules Drives Inhibition of Nuclear Import, Loss of Nuclear TDP-43, and Cell Death. Neuron 102, 339–357 e337 (2019). [PubMed: 30853299]

11. Klim JR et al., ALS-implicated protein TDP-43 sustains levels of STMN2, a mediator of motor neuron growth and repair. Nat Neurosci 22, 167–179 (2019). [PubMed: 30643292]

12. Ling JP, Pletnikova O, Troncoso JC, Wong PC, TDP-43 repression of nonconserved cryptic exons is compromised in ALS-FTD. Science 349, 650–655 (2015). [PubMed: 26250685]

13. Melamed Z et al., Premature polyadenylation-mediated loss of stathmin-2 is a hallmark of TDP-43-dependent neurodegeneration. Nat Neurosci 22, 180–190 (2019). [PubMed: 30643298]

14. Coyne AN et al., Post-transcriptional Inhibition of Hsc70–4/HSPA8 Expression Leads to Synaptic Vesicle Cycling Defects in Multiple Models of ALS. Cell Rep 21, 110–125 (2017). [PubMed: 28978466]

15. Miskiewicz K et al., HDAC6 is a Bruchpilot deacetylase that facilitates neurotransmitter release. Cell Rep 8, 94–102 (2014). [PubMed: 24981865]

16. Cohen TJ et al., An acetylation switch controls TDP-43 function and aggregation propensity. Nat Commun 6, 5845 (2015). [PubMed: 25556531]

17. Banani SF, Lee HO, Hyman AA, Rosen MK, Biomolecular condensates: organizers of cellular biochemistry. Nat Rev Mol Cell Biol 18, 285–298 (2017). [PubMed: 28225081]

18. Snead WT, Gladfelter AS, The Control Centers of Biomolecular Phase Separation: How Membrane Surfaces, PTMs, and Active Processes Regulate Condensation. Mol Cell 76, 295–305 (2019). [PubMed: 31604601]

19. Brangwynne CP et al., Germline P granules are liquid droplets that localize by controlled dissolution/condensation. Science 324, 1729–1732 (2009). [PubMed: 19460965]

20. Jain A, Vale RD, RNA phase transitions in repeat expansion disorders. Nature 546, 243–247 (2017). [PubMed: 28562589]

21. Woodruff JB et al., The Centrosome Is a Selective Condensate that Nucleates Microtubules by Concentrating Tubulin. Cell 169, 1066–1077 e1010 (2017). [PubMed: 28575670]

22. Schmidt HB, Gorlich D, Transport Selectivity of Nuclear Pores, Phase Separation, and Membraneless Organelles. Trends Biochem Sci 41, 46–61 (2016). [PubMed: 26705895]

23. Hnisz D, Shrinivas K, Young RA, Chakraborty AK, Sharp PA, A Phase Separation Model for Transcriptional Control. Cell 169, 13–23 (2017). [PubMed: 28340338]

24. Feric M et al., Coexisting Liquid Phases Underlie Nucleolar Subcompartments. Cell 165, 1686–1697 (2016). [PubMed: 27212236]

25. West JA et al., Structural, super-resolution microscopy analysis of paraspeckle nuclear body organization. J Cell Biol 214, 817–830 (2016). [PubMed: 27646274]

26. Brangwynne CP, Mitchison TJ, Hyman AA, Active liquid-like behavior of nucleoli determines their size and shape in Xenopus laevis oocytes. Proc Natl Acad Sci U S A 108, 4334–4339 (2011). [PubMed: 21368180]

27. Putnam A, Cassani M, Smith J, Seydoux G, A gel phase promotes condensation of liquid P granules in Caenorhabditis elegans embryos. Nat Struct Mol Biol 26, 220–226 (2019). [PubMed: 30833787]

28. Gallego LD et al., Phase separation directs ubiquitination of gene-body nucleosomes. Nature 579, 592–597 (2020). [PubMed: 32214243]

29. Schmidt HB, Rohatgi R, In Vivo Formation of Vacuolated Multi-phase Compartments Lacking Membranes. Cell Rep 16, 1228–1236 (2016). [PubMed: 27452472]

30. Wang C et al., Stress Induces Dynamic, Cytotoxicity-Antagonizing TDP-43 Nuclear Bodies via Paraspeckle LncRNA NEAT1-Mediated Liquid-Liquid Phase Separation. Mol Cell 79, 443–458 e447 (2020). [PubMed: 32649883]

31. Wang J et al., A Molecular Grammar Governing the Driving Forces for Phase Separation of Prion-like RNA Binding Proteins. Cell 174, 688–699 e616 (2018). [PubMed: 29961577]

32. Kelmer Sacramento E et al., Reduced proteasome activity in the aging brain results in ribosome stoichiometry loss and aggregation. Mol Syst Biol 16, e9596 (2020). [PubMed: 32558274]

33. Saez I, Vilchez D, The Mechanistic Links Between Proteasome Activity, Aging and Age-related Diseases. Curr Genomics 15, 38–51 (2014). [PubMed: 24653662]

34. Afroz T et al., Functional and dynamic polymerization of the ALS-linked protein TDP-43 antagonizes its pathologic aggregation. Nat Commun 8, 45 (2017). [PubMed: 28663553]

35. Wang A et al., A single N-terminal phosphomimic disrupts TDP-43 polymerization, phase separation, and RNA splicing. EMBO J 37, (2018).

36. Moreno F et al., A novel mutation P112H in the TARDBP gene associated with frontotemporal lobar degeneration without motor neuron disease and abundant neuritic amyloid plaques. Acta Neuropathol Commun 3, 19 (2015). [PubMed: 25853458]

37. Chen HJ et al., RRM adjacent TARDBP mutations disrupt RNA binding and enhance TDP-43 proteinopathy. Brain 142, 3753–3770 (2019). [PubMed: 31605140]

38. Kovacs GG et al., TARDBP variation associated with frontotemporal dementia, supranuclear gaze palsy, and chorea. Mov Disord 24, 1843–1847 (2009). [PubMed: 19609911]

39. Elden AC et al., Ataxin-2 intermediate-length polyglutamine expansions are associated with increased risk for ALS. Nature 466, 1069–1075 (2010). [PubMed: 20740007]

40. Vo N, Goodman RH, CREB-binding protein and p300 in transcriptional regulation. J Biol Chem 276, 13505–13508 (2001). [PubMed: 11279224]

41. Cohen TJ, Lee VM, Trojanowski JQ, TDP-43 functions and pathogenic mechanisms implicated in TDP-43 proteinopathies. Trends Mol Med 17, 659–667 (2011). [PubMed: 21783422]

42. Flores BN et al., An Intramolecular Salt Bridge Linking TDP43 RNA Binding, Protein Stability, and TDP43-Dependent Neurodegeneration. Cell Rep 27, 1133–1150 e1138 (2019). [PubMed: 31018129]

43. Pelzl G, Hauser A, Birefringence and phase transitions in liquid crystals. Phase Transitions 37, 33–62 (1991).

44. Oldenbourg R, Polarized light microscopy: principles and practice. Cold Spring Harb Protoc 2013, (2013).

45. Reyes Mateo C, Ulises Acuna A, Brochon JC, Liquid-crystalline phases of cholesterol/lipid bilayers as revealed by the fluorescence of trans-parinaric acid. Biophys J 68, 978–987 (1995). [PubMed: 7756560]

46. Liu K et al., Thermotropic liquid crystals from biomacromolecules. Proc Natl Acad Sci U S A 111, 18596–18600 (2014). [PubMed: 25512508]

47. Rog O, Kohler S, Dernburg AF, The synaptonemal complex has liquid crystalline properties and spatially regulates meiotic recombination factors. Elife 6, (2017).

48. Ayala YM et al., TDP-43 regulates its mRNA levels through a negative feedback loop. EMBO J 30, 277–288 (2011). [PubMed: 21131904]

49. Saha S et al., Polar Positioning of Phase-Separated Liquid Compartments in Cells Regulated by an mRNA Competition Mechanism. Cell 166, 1572–1584 e1516 (2016). [PubMed: 27594427]

50. Bracha D et al., Mapping Local and Global Liquid Phase Behavior in Living Cells Using Photo-Oligomerizable Seeds. Cell 175, 1467–1480 e1413 (2018). [PubMed: 30500534]

51. Vargas JD, Hatch EM, Anderson DJ, Hetzer MW, Transient nuclear envelope rupturing during interphase in human cancer cells. Nucleus 3, 88–100 (2012). [PubMed: 22567193]

52. Patel A et al., A Liquid-to-Solid Phase Transition of the ALS Protein FUS Accelerated by Disease Mutation. Cell 162, 1066–1077 (2015). [PubMed: 26317470]

53. Conicella AE et al., TDP-43 alpha-helical structure tunes liquid-liquid phase separation and function. Proc Natl Acad Sci U S A 117, 5883–5894 (2020). [PubMed: 32132204]

54. Mompean M et al., Point mutations in the N-terminal domain of transactive response DNA-binding protein 43 kDa (TDP-43) compromise its stability, dimerization, and functions. J Biol Chem 292, 11992–12006 (2017). [PubMed: 28566288]

55. Shiina Y, Arima K, Tabunoki H, Satoh J, TDP-43 dimerizes in human cells in culture. Cell Mol Neurobiol 30, 641–652 (2010). [PubMed: 20043239]

56. Gasior K et al., Partial demixing of RNA-protein complexes leads to intradroplet patterning in phase-separated biological condensates. Phys Rev E 99, 012411 (2019). [PubMed: 30780260]

57. Palleros DR, Welch WJ, Fink AL, Interaction of hsp70 with unfolded proteins: effects of temperature and nucleotides on the kinetics of binding. Proc Natl Acad Sci U S A 88, 5719–5723 (1991). [PubMed: 1829527]

58. Rosenzweig R, Nillegoda NB, Mayer MP, Bukau B, The Hsp70 chaperone network. Nat Rev Mol Cell Biol 20, 665–680 (2019). [PubMed: 31253954]

59. Williamson DS et al., Novel adenosine-derived inhibitors of 70 kDa heat shock protein, discovered through structure-based design. J Med Chem 52, 1510–1513 (2009). [PubMed: 19256508]

60. D'Angelo MA, Raices M, Panowski SH, Hetzer MW, Age-dependent deterioration of nuclear pore complexes causes a loss of nuclear integrity in postmitotic cells. Cell 136, 284–295 (2009). [PubMed: 19167330]

61. Gibson BA et al., Organization of Chromatin by Intrinsic and Regulated Phase Separation. Cell 179, 470–484 e421 (2019). [PubMed: 31543265]

62. Lukavsky PJ et al., Molecular basis of UG-rich RNA recognition by the human splicing factor TDP-43. Nat Struct Mol Biol 20, 1443–1449 (2013). [PubMed: 24240615]

63. Ganassi M et al., A Surveillance Function of the HSPB8-BAG3-HSP70 Chaperone Complex Ensures Stress Granule Integrity and Dynamism. Mol Cell 63, 796–810 (2016). [PubMed: 27570075]

64. Frottin F et al., The nucleolus functions as a phase-separated protein quality control compartment. Science 365, 342–347 (2019). [PubMed: 31296649]

65. Alshareedah I, Moosa MM, Raju M, Potoyan DA, Banerjee PR, Phase transition of RNA-protein complexes into ordered hollow condensates. Proc Natl Acad Sci U S A 117, 15650–15658 (2020). [PubMed: 32571937]

66. Banerjee PR, Milin AN, Moosa MM, Onuchic PL, Deniz AA, Reentrant Phase Transition Drives Dynamic Substructure Formation in Ribonucleoprotein Droplets. Angew Chem Int Ed Engl 56, 11354–11359 (2017). [PubMed: 28556382]

67. Illmensee K, Mahowald AP, Loomis MR, The ontogeny of germ plasm during oogenesis in Drosophila. Dev Biol 49, 40–65 (1976). [PubMed: 815119]

68. Kistler KE et al., Phase transitioned nuclear Oskar promotes cell division of Drosophila primordial germ cells. Elife 7, (2018).

69. Narcis JO et al., Accumulation of poly(A) RNA in nuclear granules enriched in Sam68 in motor neurons from the SMNDelta7 mouse model of SMA. Sci Rep 8, 9646 (2018). [PubMed: 29941967]

70. Gallego-Iradi MC et al., N-terminal sequences in matrin 3 mediate phase separation into droplet-like structures that recruit TDP43 variants lacking RNA binding elements. Lab Invest 99, 1030–1040 (2019). [PubMed: 31019288]

71. Ling SC, Polymenidou M, Cleveland DW, Converging mechanisms in ALS and FTD: disrupted RNA and protein homeostasis. Neuron 79, 416–438 (2013). [PubMed: 23931993]

72. Neumann M et al., Ubiquitinated TDP-43 in frontotemporal lobar degeneration and amyotrophic lateral sclerosis. Science 314, 130–133 (2006). [PubMed: 17023659]

73. Robinson JL et al., Neurodegenerative disease concomitant proteinopathies are prevalent, age-related and APOE4-associated. Brain 141, 2181–2193 (2018). [PubMed: 29878075]

74. Yang HS et al., Evaluation of TDP-43 proteinopathy and hippocampal sclerosis in relation to APOE epsilon4 haplotype status: a community-based cohort study. Lancet Neurol 17, 773–781 (2018). [PubMed: 30093249]

75. Josephs KA et al., TDP-43 is a key player in the clinical features associated with Alzheimer's disease. Acta Neuropathol 127, 811–824 (2014). [PubMed: 24659241]

76. Van Helleputte L et al., Inhibition of histone deacetylase 6 (HDAC6) protects against vincristine-induced peripheral neuropathies and inhibits tumor growth. Neurobiol Dis 111, 59–69 (2018). [PubMed: 29197621]

77. Mauermann ML, Blumenreich MS, Dispenzieri A, Staff NP, A case of peripheral nerve microvasculitis associated with multiple myeloma and bortezomib treatment. Muscle Nerve 46, 970–977 (2012). [PubMed: 23225391]

78. Palanca A, Casafont I, Berciano MT, Lafarga M, Reactive nucleolar and Cajal body responses to proteasome inhibition in sensory ganglion neurons. Biochim Biophys Acta 1842, 848–859 (2014). [PubMed: 24269586]

79. Gibson DG et al., Enzymatic assembly of DNA molecules up to several hundred kilobases. Nat Methods 6, 343–345 (2009). [PubMed: 19363495]

80. Schmidt HB, Barreau A, Rohatgi R, Phase separation-deficient TDP43 remains functional in splicing. Nat Commun 10, 4890 (2019). [PubMed: 31653829]

81. Martinez FJ et al., Protein-RNA Networks Regulated by Normal and ALS-Associated Mutant HNRNPA2B1 in the Nervous System. Neuron 92, 780–795 (2016). [PubMed: 27773581]

82. Burkhardt MF et al., A cellular model for sporadic ALS using patient-derived induced pluripotent stem cells. Mol Cell Neurosci 56, 355–364 (2013). [PubMed: 23891805]

83. Chambers SM et al., Highly efficient neural conversion of human ES and iPS cells by dual inhibition of SMAD signaling. Nat Biotechnol 27, 275–280 (2009). [PubMed: 19252484]

84. Vives-Bauza C et al., PINK1-dependent recruitment of Parkin to mitochondria in mitophagy. Proc Natl Acad Sci U S A 107, 378–383 (2010). [PubMed: 19966284]

85. Schwoebel ED, Ho TH, Moore MS, The mechanism of inhibition of Ran-dependent nuclear transport by cellular ATP depletion. J Cell Biol 157, 963–974 (2002). [PubMed: 12058015]

86. Mastronarde DN, Automated electron microscope tomography using robust prediction of specimen movements. J Struct Biol 152, 36–51 (2005). [PubMed: 16182563]

87. Zheng SQ et al., MotionCor2: anisotropic correction of beam-induced motion for improved cryo-electron microscopy. Nat Methods 14, 331–332 (2017). [PubMed: 28250466]

88. Mastronarde DN, Held SR, Automated tilt series alignment and tomographic reconstruction in IMOD. J Struct Biol 197, 102–113 (2017). [PubMed: 27444392]

89. Yuan ZF et al., pParse: a method for accurate determination of monoisotopic peaks in high-resolution mass spectra. Proteomics 12, 226–235 (2012). [PubMed: 22106041]

90. Chi H et al., Comprehensive identification of peptides in tandem mass spectra using an efficient open search engine. Nat Biotechnol, (2018).

91. Liu C et al., pQuant improves quantitation by keeping out interfering signals and evaluating the accuracy of calculated ratios. Anal Chem 86, 5286–5294 (2014). [PubMed: 24799117]

92. Gasior K, Newby J, Gladfelter AS, Mathematical Modeling of liquid-liquid phase separation of TDP-43. (2020).

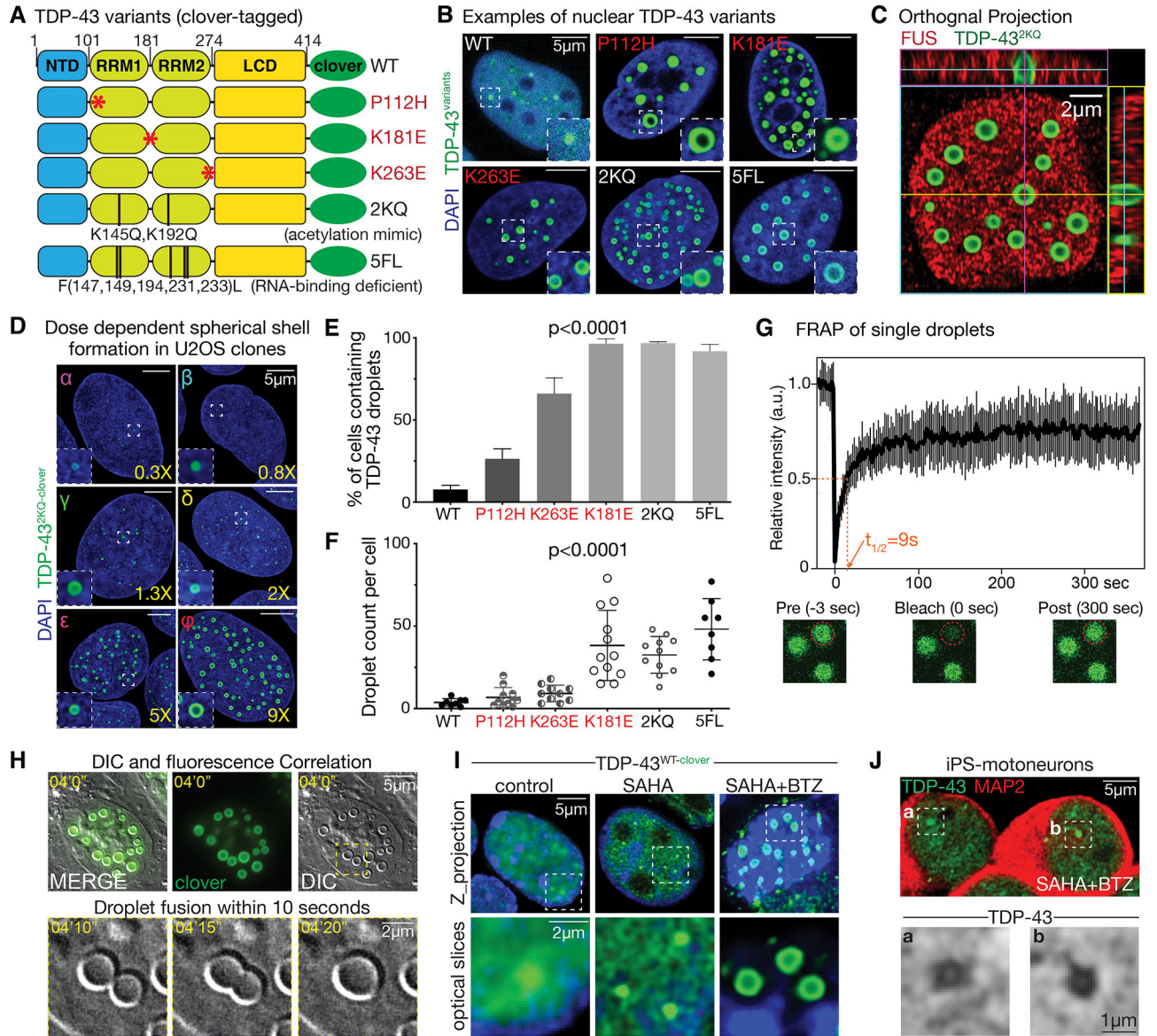93. Zhao J, Mathematical Modeling of RNA-protein complexes under partial demixing conditions. (2017).

**Fig. 1. RNA-binding deficient TDP-43 naturally de-mixes into intranuclear liquid spherical shells.**

(**A**) Schematic of TDP-43 wildtype and mutant proteins. All proteins were tagged at the carboxyl-terminus with the bright GFP variant, clover. (**B**) U2OS cells induced to express TDP-43 variants develop many more nuclear droplets than do cells expressing wildtype TDP-43. (*Dashed boxes*) Examples of nuclear droplets and magnified at the lower right corners. (**C**) Orthogonal projections demonstrate that TDP-43$^{2KQ\text{-}clover}$ droplets have nearly perfectly round spherical shells. (**D**) Spherical shell formation is dose dependent. (*Lower right*) TDP-43$^{2KQ\text{-}clover}$ expression level (relative to endogenous TDP-43) in each clone (determined as in Fig. S1C–F) is marked at the lower right of each image. (**E-F**) Quantified percentages of cells containing (**E**) TDP-43 droplets and (**F**) number of nuclear droplets per cell in U2OS cells expressing clover-tagged TDP-43 variants. (**G**) Liquid-like character of intranuclear TDP-43$^{2KQ\text{-}clover}$ spherical shells, demonstrated by rapid fluorescence recovery

after photobleaching (FRAP). (**H**) Dynamic fusion of TDP-43$^{2KQ\text{-}clover}$ spherical shells visualized by live cell differential interference contrast (DIC) microscopy. Two spherical shells (1–2μm) fuse into one (>2 μm) within 10 seconds. Inhibition of HDAC and proteasome activity synergize to enhance TDP-43 anisosome formation in neuron-like SHSY-5Y cells (**I**) and in iPSC-derived motor neurons (**J**).
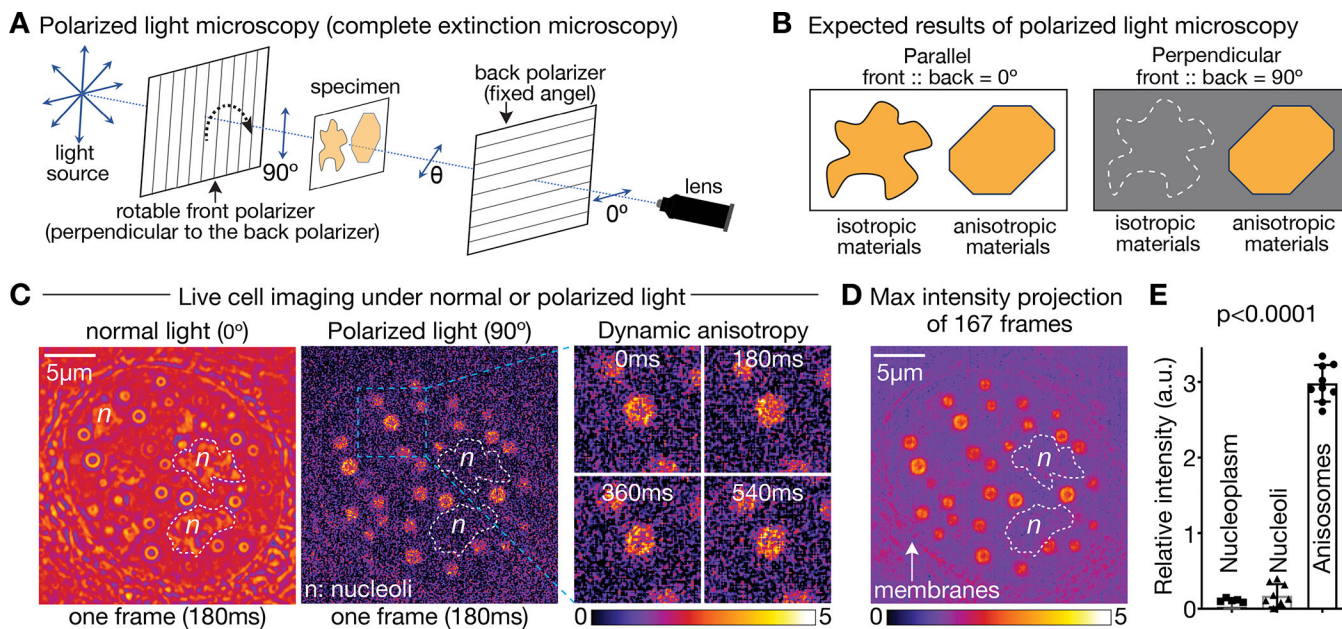
**Fig. 2. TDP-43 intranuclear liquid spherical shells are anisotropic compartments of anisosomes.** (**A**) Schematic of complete extinction microscopy. The light path contains two polarizers: the front polarizer can be adjusted from 0° to 90°, and the back polarizer has a fixed angle. Rotating the front polarizer result in a change of polarized light. (**B**) Only anisotropic materials can be distinguished by complete extinction microscopy because the birefringent property of the anisotropic material allows some light to pass the back polarizer. (**C**) The same nucleus containing TDP-43 liquid spherical shells is imaged under normal or polarized light sources (images are pseudocolored to display intensity of light). Phase-separated nucleoli (marked by "*n*") cannot be detected when the polarized light is perpendicular to the filter. (*Dashed box*) Magnified view of the dynamic anisotropic sub-domains. (**D**) Maximum intensity projection of images in (**C**) (167 frames in 30 seconds of live imaging under complete extinction conditions). Arrow points to membranes, a known anisotropic structure – the lipid bilayer. (**E**) Quantification of signal intensity of nucleoplasm, nucleoli, and anisosomes.
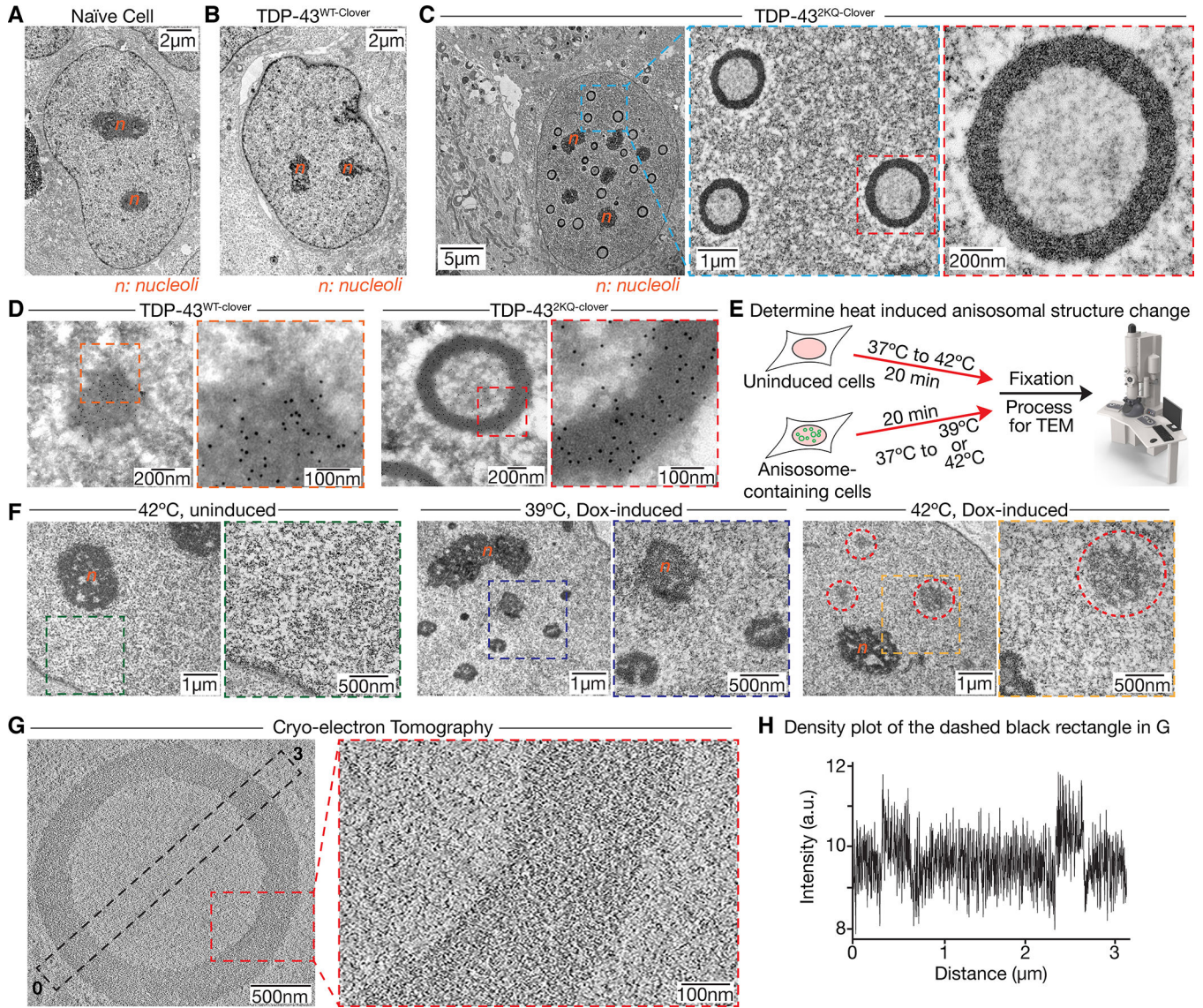
**Fig. 3. TDP-43 anisosomes are membraneless compartments with densely packed shells visualized by transmission electron microscopy (TEM) and cryo-electron tomography (CryoET).**
TEM examples of nuclei from (**A**) a naïve U2OS cell, (**B**) a U2OS cell expressing TDP-43[WT-clover], and (**C**) a U2OS cell expressing TDP-43[2KQ-clover] (see additional examples in Fig. S3). (**D**) Immunogold labeling with a GFP antibody of (*left*) a TDP-43[WT-clover] droplet or (*right*) a TDP-43[2KQ-clover] anisosome. (*Dashed boxes*) Enlarged views of the distribution of gold particles (see Fig. S4 for additional examples). (**E**) Schematic of 20-minute temperature shift and determination of the structural changes with TEM. (**F**) A temperature shift-induced structural change visualized by TEM. (*Dashed boxes*) Magnified views of each condition. At 42°C, no irregular structure was observed in the nucleoplasm without the induction of anisosomes. At 39 °C, anisosomes become irregular shape, while at 42 °C, irregular shape and less electron dense. (Dashed r*ed circles*) Irregular electron dense compartments. (**G**) Cryo-electron tomography of an anisosome and (**H**) density plot of the area enclosed in the dashed black rectangle.
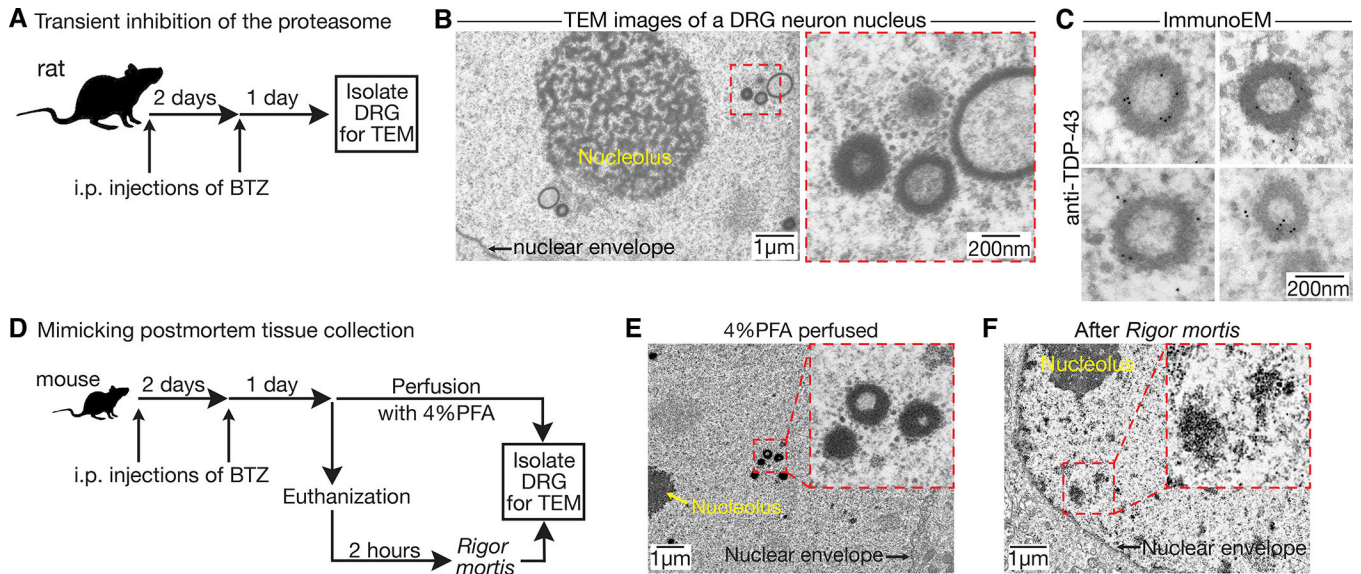
**Fig. 4. Proteolytic stress in neurons of the adult nervous system induces TDP-43-containing anisosomes, which convert into aggregates as ATP levels fall.**

(**A**) Schematic of experimental steps for inducing transient proteolytic stress in Sprague Dawley rats by intravenous (i.v.) administration of the proteasome inhibitor bortezomib (BTZ). (**B**) TEM images of intranuclear spherical shells found in nuclei of DRG sensory neurons from mice treated as in (**A**). (*Dashed red square*) area magnified at right. (**C**) Immunogold labelling for endogenous TDP-43 in bortezomib-induced spherical shells. (**D**) Schematic of induction of TDP-43-containing spherical shells in mouse DRG neurons by partial proteasome inhibition and then examined after immediate or delayed tissue collection. Images of DRGs collected (**E**) immediately after perfusion or (**F**) after a 2-hour postmortem delay during which ATP levels falls sufficiently to initiate rigor mortis. Anisosomes seen in freshly fixed samples convert to amorphous dense intranuclear structures after postmortem delay.
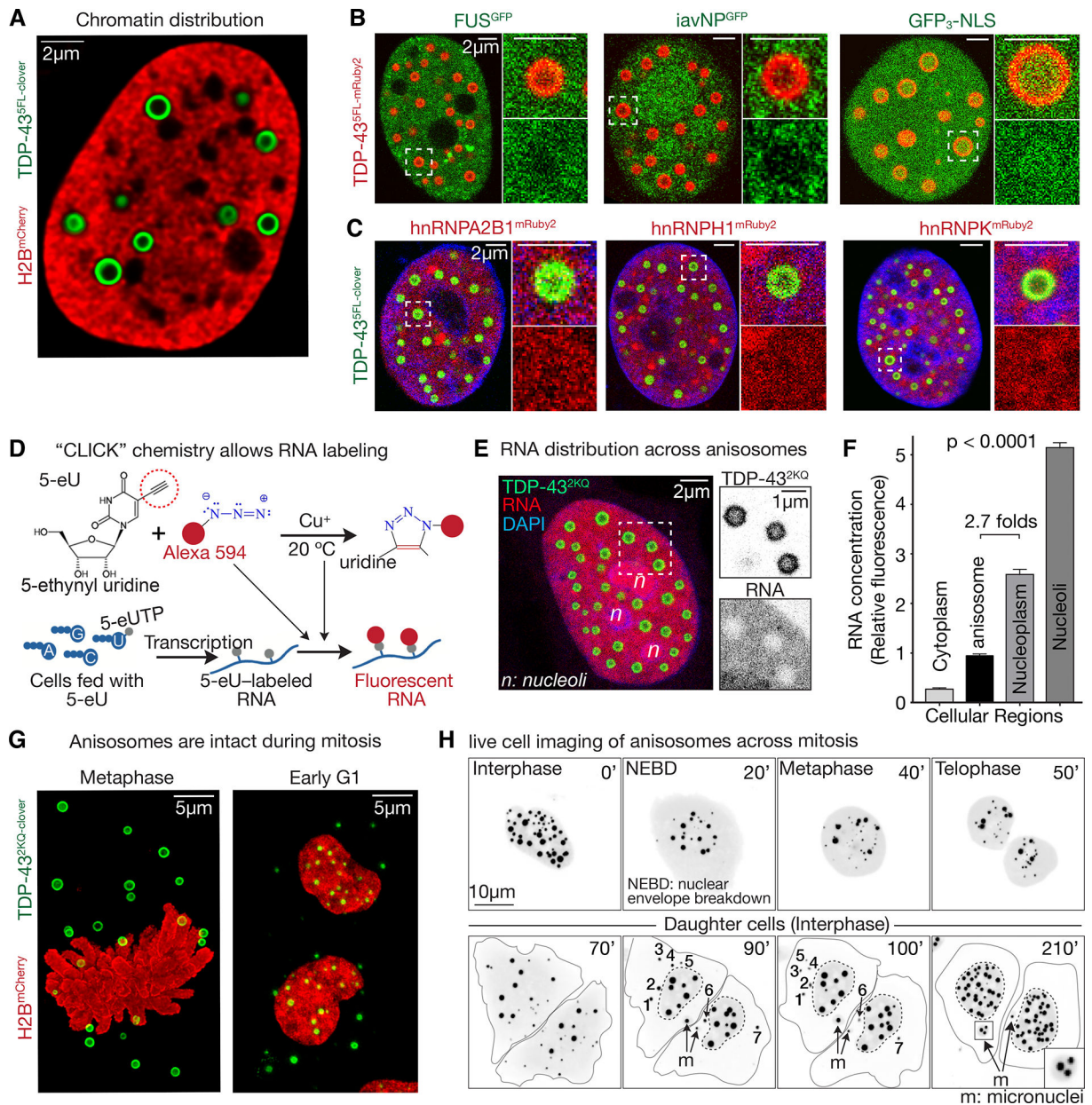
**Fig. 5. TDP-43 anisosomes, intact during mitosis, are selective barriers for RNA and some nuclear proteins.**

(**A**) A U2OS nucleus stably expressing H2B[mCherry], a fluorescent histone marker and TDP-43[5FL-clover]. (**B,C**) Fluorescence imaging of nuclear RNA-binding proteins (**B**) hnRNPA2B1, hnRNPH1 and hnRNPK (each carboxy-terminally tagged with mRuby2) or (**C**) EGFP-labeled FUS, iavNP or EGFP alone. (**D**) Schematic for fluorescent labeling of cellular RNA with "CLICK" chemistry. (**E**) Imaging of anisosomes of TDP-43[2KQ] and nuclear RNA (labeled as in (**D**)). (**F**) Quantification of fluorescence intensity of the RNA in (**E**). (**G**) Imaging of TDP-43 anisosomes in mitotic and post-mitotic cytoplasm and post-mitotic reassembly within daughter nuclei. (**H**) An imaging series of TDP-43[2KQ-clover] anisosomes during mitosis and early interphase. (Solid lines) The cell plasma membrane;

(dashed lines) outline of the nuclear envelope. The numbers 1–7 denote specific cytoplasmic TDP-43$^{2KQ\text{-}clover}$ droplets, each of which becomes smaller within 10 minutes. (*m*) Anisosomes reforming within micronuclei produced by mitotic chromosome segregation errors.
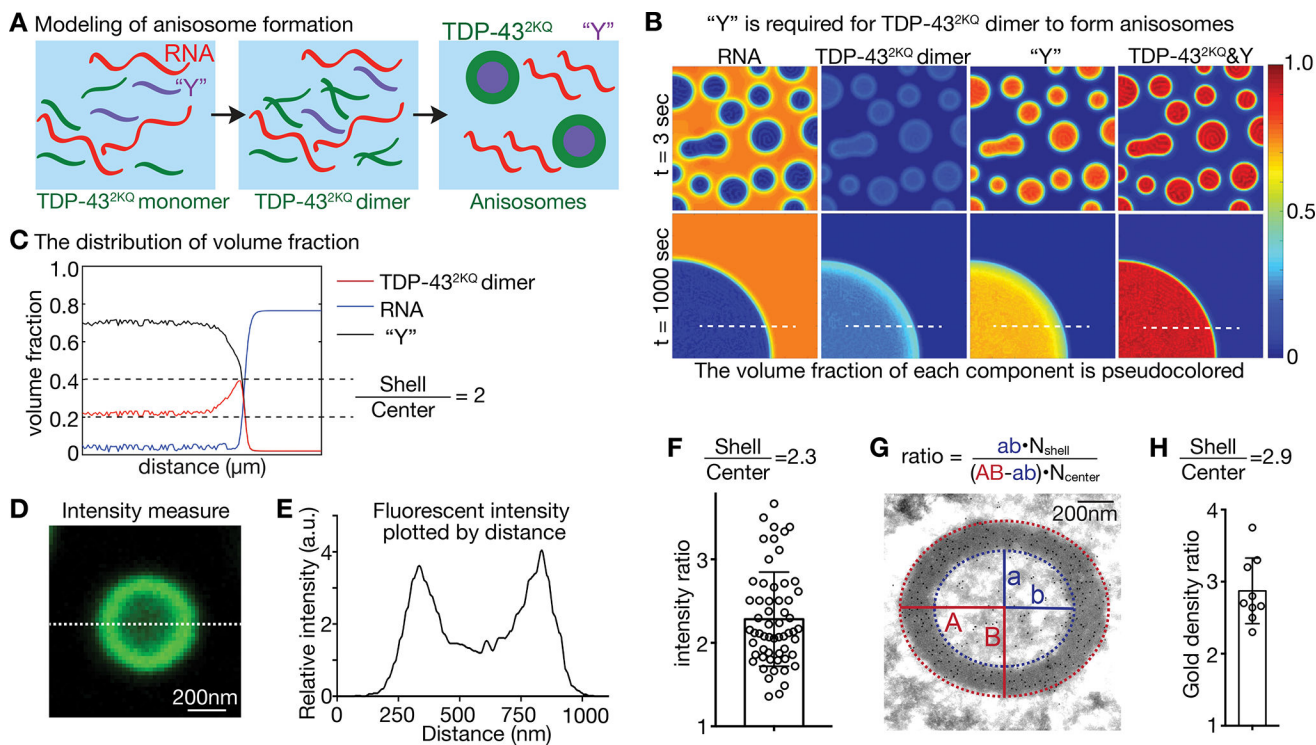
**Fig. 6. Mathematical modeling predicts that a third component is required for anisosomal formation and maintenance.**

(**A**) Schematic of modeling of anisosome formation by TDP-43[2KQ] mutant in a simple mixture of TDP-43, RNA, and a proposed Y molecule that has high affinity for itself, low affinity for TDP-43, and no RNA binding. (**B**) A snapshot from the model in (**A**) of demixing at 3 and 1000 seconds after starting from a uniform solution. (**C**) The volume fraction of each species from modeling in (**A and B**) at a 1000 second time point. The ratio of volume fraction between the shell and the center of the anisosome for TDP-43[2KQ] is about 2. Clover fluorescence intensity across TDP-43[2KQ] anisosomes. (**D**) An optical slice of an anisosome with (**E**) intensity of the dashed line in (**D**). (**F**) The quantified ratio between the shell and the center, with a mean of $2.28 \pm 0.56$ (SD). (**G**) Measurement of the ratio of gold particle density in immunogold-labeling of TDP-43[2KQ-clover] in an anisosome and (**H**) quantification of the ratio of gold particle density between the shell and the center.
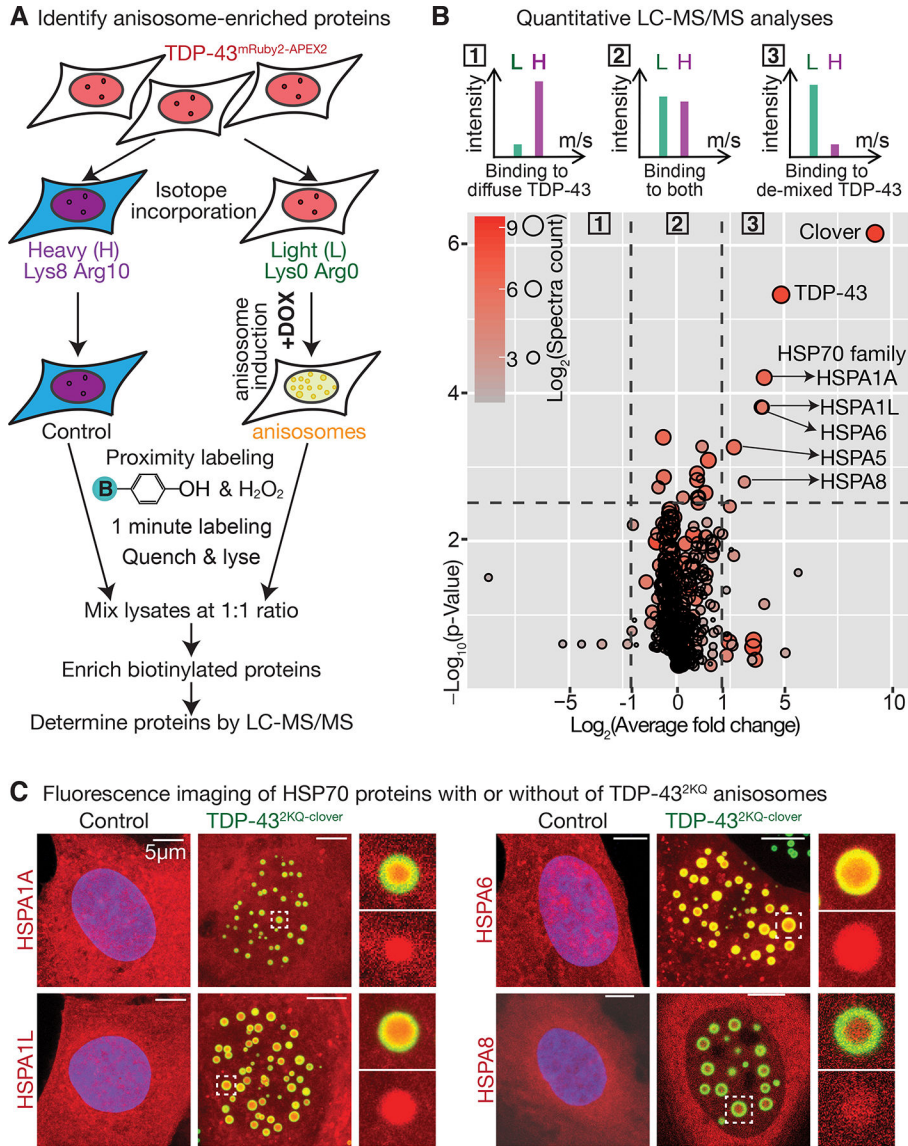
**Fig. 7. The HSP70 family of molecular chaperones are specifically enriched in cores of TDP-43 anisosomes.**

(**A**) Schematic of APEX2-mediated proximity labeling followed by quantitative proteomic analyses (see also Fig. S10). (**B**) Quantitative proteomic analyses identify HSP70 family proteins to be enriched in the cores of de-mixed TDP-43 anisosomes. Y axis is p-value at $\log_{10}$ scale; X axis is fold enrichment on $\log_2$ scale. The size and color of each spot correspond to the total spectral counts of LC/MS-MS reads on $\log_2$ scale. (**C**) Maximum intensity projections of immunofluorescence images of U2OS nuclei expressing (*green*) TDP-43$^{2KQ-clover}$ anisosomes and (*red*) HSP70 family proteins tagged by mRuby2. (*White boxes*) Boxed areas that are magnified at right.
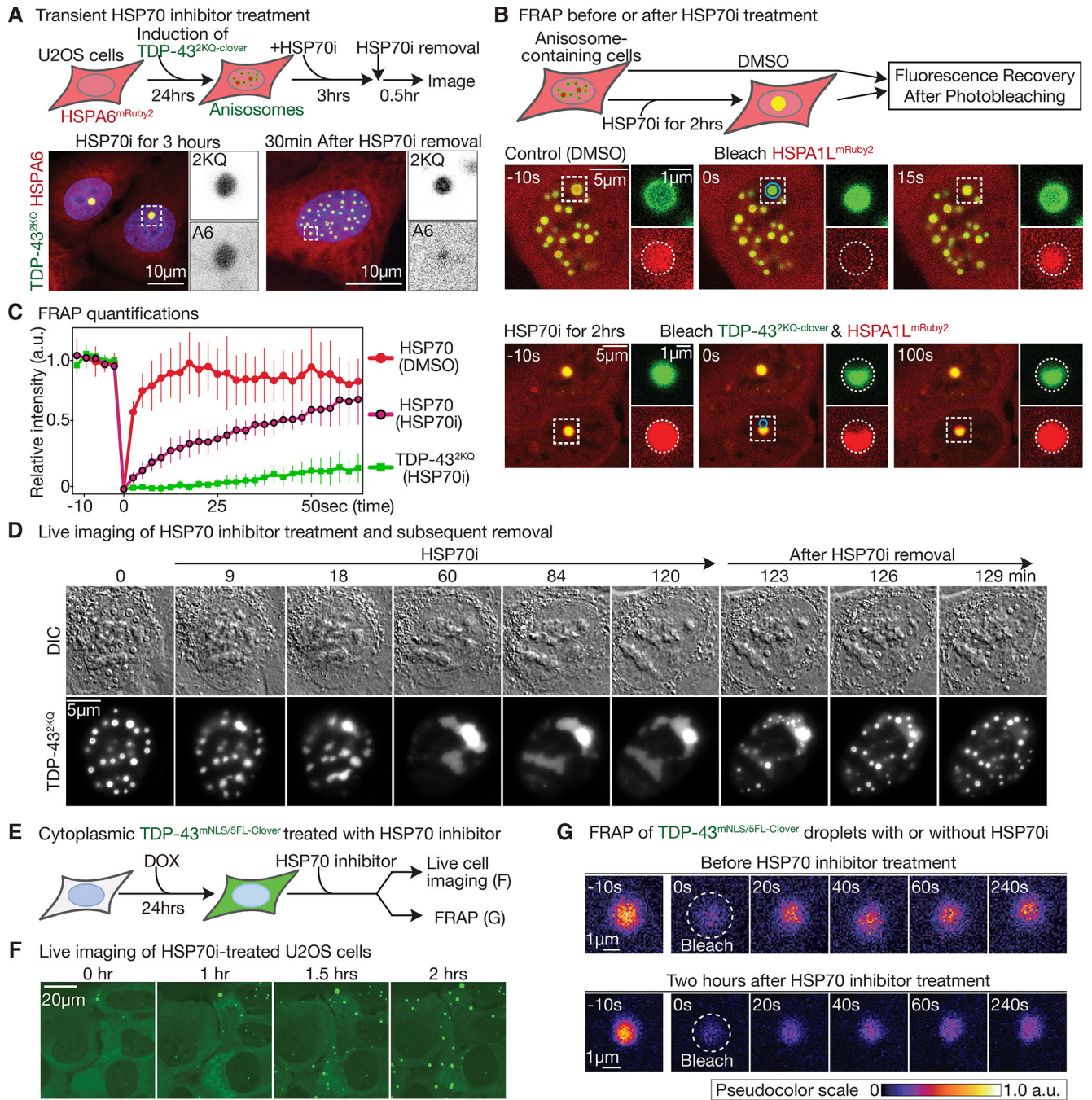
**Fig. 8. The ATP-dependent chaperone activity of the HSP70 family chaperones regulate anisosomal structure and liquidity of both shells and cores.**

(**A**) Imaging of anisosomes formed after transient induction of TDP-43[2KQ-clover] in cells stably expressing HSPA6[mRuby2] after (*left*) addition of an HSP70 ATPase inhibitor (VER155008) and (*right*) after a subsequent 0.5 hour wash out of the inhibitor. (**B**) (*Top*) Schematic of FRAP of anisosomes formed in cells in (**A**) in the absence of or after addition the HSP70 inhibitor. (*Middle*) FRAP of HSPA1L[mRuby2] in TDP-43[2KQ-clover] anisosomes. (*Bottom*) FRAP of a portion of a TDP-43[2KQ-clover] and HSPA1L[mRuby2]-containing

intranuclear droplet in cells treated with the HSP70 inhibitor. (**C**) Kinetics of the FRAP experiments in (**B**). HSP70$^{mRuby2}$ quickly recovers after bleaching (the red curve, $\tau < 2$ seconds), but is much less dynamic after HSP70 inhibitor treatment (the purple curve, $\tau$ is between 40 and 42.5 seconds). In the HSP70 inhibitor, only a small proportion of TDP-43$^{2KQ\text{-}clover}$ recovers, which recovers slowly. (**D**) Live DIC and fluorescence imaging of TDP-43$^{2KQ\text{-}clover}$ in anisosomes after addition and wash out of the HSP70 inhibitor. (**E**) Schematic of addition and imaging of diffuse cytoplasmic TDP-43$^{NLSm/5FL\text{-}clover}$ after addition of the HSP70 inhibitor. (**F**) Live fluorescence imaging of TDP-43$^{NLSm/5FL\text{-}clover}$ assembly into cytoplasmic droplets upon addition of the HSP70 inhibitor. (**G**) FRAP of cytoplasmic droplets from (**F**)
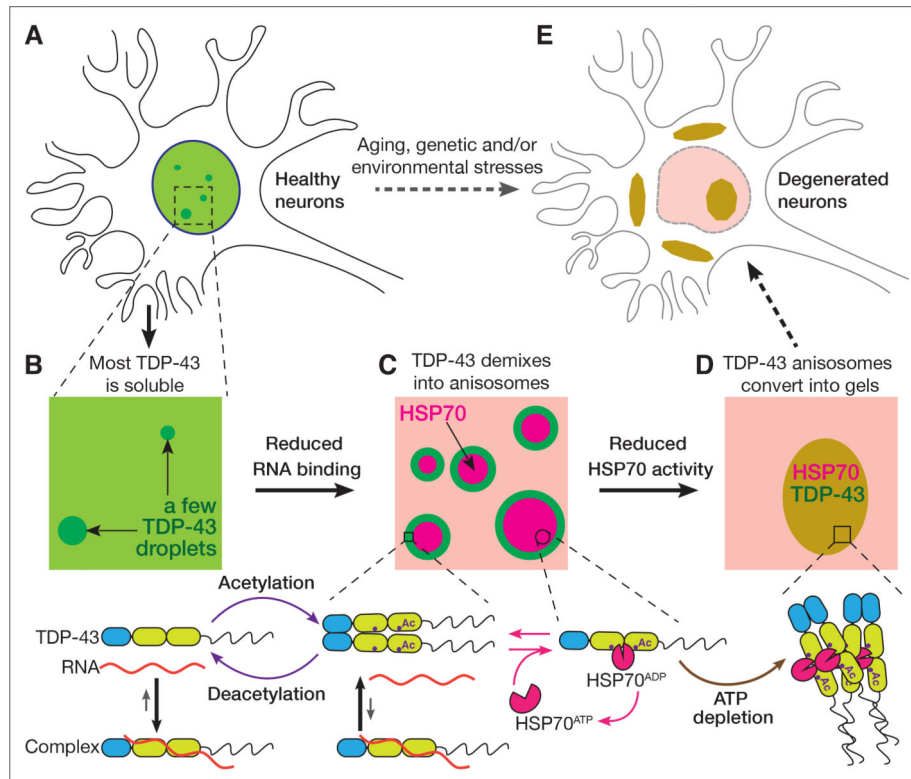
**TDP-43 phase transition is regulated by its RNA affinity and HSP70 activity**
RNA-binding protein TDP-43 forms aggregates in degenerating neurons, a pathological feature associated with aging, genetic, and/or environmental factors. Although naturally demixed, RNA-binding proficient TDP-43 is largely soluble in the nucleus with a small proportion demixed (**A** and **B**). Its RNA affinity is eliminated by acetylation, which drives most of TDP-43 into anisosomes, an intranuclear membraneless compartment with symmetrically aligned shell and core in which RNA-free TDP-43 is enriched in the shell. HSP70 stabilizes RNA-free TDP-43 and is enriched in the anisosomal core (**C**). When ATP-dependent chaperone activity of HSP70 is reduced by ATP depletion TDP-43 anisosomes collapse into gels (**D**) which may be precursors of intranuclear and cytoplasmic aggregates observed in degenerating neurons (**E**).